CZECH TECHNICAL UNIVERSITY IN PRAGUE

Faculty of Nuclear Sciences and Physical Engineering

Department of Physics

Master's thesis

Exclusive photon-induced production at the LHC accelerator

Bc. Filip Nechanský

Supervisor: Mgr. Oldřich Kepka, Ph.D.

Prague, 2017

ČESKÉ VYSOKÉ UČENÍ TECHNICKÉ
V PRAZE
Fakulta Jaderná a Fyzikálně Inženýrská
Katedra Fyziky

Diplomová práce

Exkluzivní fotonem indukovaná produkce na urychlovači LHC

Bc. Filip Nechanský

Supervisor: Mgr. Oldřich Kepka, Ph.D.

Praha, 2017

ČESKÉ VYSOKÉ UČENÍ TECHNICKÉ V PRAZE
FAKULTA JADERNÁ A FYZIKÁLNĚ INŽENÝRSKÁ
PRAHA 1 - STARÉ MĚSTO, BŘEHOVÁ 7 - PSČ 115 19

Katedra: fyziky *Akademický rok:* 2016/2017

ZADÁNÍ DIPLOMOVÉ PRÁCE

Student: Bc. Filip Nechanský

Studijní program: Aplikace přírodních věd

Obor: Experimentální jaderná a částicová fyzika

Název práce: (česky) Exkluzivní fotonem indukovaná produkce na urychlovači LHC

Název práce: (anglicky) Exclusive photon-induced production at the LHC accelerator

Pokyny pro vypracování:

1) Seznamte se s existujícími měřeními exkluzivní produkce na LHC a s teorií fotonových interakcí.

2) Na základě minulých měření a pomocí Monte-Carlo dat navrhněte měření fotonem indukované produkce pro těžišťovou energii 13 TeV.

3) Napište program sloužící k analýze exkluzivních událostí, optimalizujte selekci zajímavých událostí a implementujte potřebné korekce.

4) Výsledky diskutujte a zasaďte do kontextu již provedených měření.

Doporučená literatura:

[1] CMS Collaboration: Exclusive photon-photon production of muon pairs in proton-proton collisions at sqrt(s) = 7 TeV, JHEP 01, 052 (2012)

[2] CMS Collaboration: Study of exclusive two-photon production of W(+)W(-) in pp collisions at sqrt(s) = 7 TeV and constraints on anomalous quartic gauge couplings, JHEP 07, 116 (2013)

[3] M. Dyndal, L. Schoeffel: The role of finite-size effects on the spectrum of equivalent photons in proton–proton collisions at the LHC, Phys. Lett. B 741, 66 (2015)

[4] ATLAS Collaboration: Measurement of exclusive gamma gamma to W(+)W(-) production and search for exclusive Higgs boson production in pp collisions at sqrt(s) = 8 TeV using the ATLAS detector, Phys. Rev. D 94, 032011 (2016)

Jméno a pracoviště vedoucího diplomové práce:

Mgr. Oldřich Kepka, Ph.D., Fyzikální ústav, Oddělení teorie a fenomenologie částic, AV ČR, v.v.i., Praha

Datum zadání diplomové práce: 20.10.2016

Termín odevzdání diplomové práce: 05.05.2017

Doba platnosti zadání je dva roky od data zadání.

....

vedoucí katedry *děkan*

ČESKÉ VYSOKÉ UČENÍ TECHNICKÉ V PRAZE
Fakulta jaderná a fyzikálně inženýrská
-1-

V Praze dne 20.10.2016

Prohlášení:

Prohlašuji, že jsem svou diplomovou práci vypracoval samostatně a použil jsem pouze podklady (literaturu, software, atd.) uvedené v přiloženém seznamu.

Nemám závažný důvod proti užití tohoto školního díla ve smyslu 60 Zákona .121/2000 Sb., o právu autorském, o právech souvisejících s právem autorským a o změně některých zákonů (autorský zákon).

V Praze dne

Title:
Exclusive photon-induced production at the LHC accelerator

Author: Bc. Filip Nechanský

Specialization: Experimental nuclear and particle physics

Sort of project: Diploma thesis

Supervisor: Mgr. Oldřich Kepka, Ph.D.

Abstract:
In proton-proton collisions, quasi-real photons emitted by colliding protons can interact and produce various final states. These photon interactions provide a unique opportunity to test the Standard Model in a clean channel. The first measurement of exclusive WW production at $\sqrt{s} = 13$ TeV is performed using 33.3 fb^{-1} of data collected with the ATLAS detector. A fiducial cross-section in the $e\mu$ final state is found to be $\sigma^{\text{Excl.,fid.}}_{\gamma\gamma\to W^+W^-\to e^\pm\mu^\mp} = 3.9 \pm 1.2\ (\text{stat}) \pm 0.4\ (\text{syst})$ fb and is compared with the Standard Model prediction based on Equivalent Photon Approximation. Theoretical calculations of the photon-induced processes must include absorptive effects in order to describe data. These effects, described by a survival factor, are measured in $\mu^+\mu^-$ final state at 13 TeV using 3.2 fb^{-1} collected in 2015. The measured cross-section is $\sigma^{\text{excl. fid.}}_{\gamma\gamma\to\mu^+\mu^-} = 3.22 \pm 0.07\ (\text{stat}) \pm 0.10\ (\text{syst})$ pb, giving a survival factor $S^{\text{excl}}_{\gamma\gamma\to\mu\mu} = 0.883 \pm 0.020$ (stat).

Key words: exclusive photon-induced processes, dilepton production, diboson production, ATLAS experiment

Název práce:
Exkluzivní fotonem indukovaná produkce na urychlovači LHC

Autor: Bc. Filip Nechanský

Abstrakt:
V proton-protonových kolizích jsou emitovány kvazi-reálné fotony a jejich interakce může produkovat různé finální stavy. Tyto fotonové interakce poskytují unikátní příležitost k testování Standartního Modelu v čistém kanále. První měření exkluzivní produkce WW pro $\sqrt{s} = 13$ TeV je provedeno pomocí 33.3 fb^{-1} dat nasbíraných detektorem ATLAS. Účinný průřez finálního stavu $e\mu$ je $\sigma^{\text{Excl.,fid.}}_{\gamma\gamma\to W^+W^-\to e^\pm\mu^\mp} = 3.9 \pm 1.2$ (stat) $\pm\, 0.4$ (syst) fb a je porovnán s předpovědí Standardního modelu založenou na Ekvivalentní Fotonové Aproximaci. Aby popisoval data musí teoretický výpočet fotononem indukovaných procesů zahrnovat absorbční efekty. Tyto efekty, popsané faktorem přežití, byly měřeny ve finálním stavu $\mu^+\mu^-$ pro 13 TeV s použitím 3.2 fb^{-1} nasbíraných v roce 2015. Naměřený účinný průřez je $\sigma^{\text{excl. fid.}}_{\gamma\gamma\to\mu^+\mu^-} = 3.22 \pm 0.07$ (stat) $\pm\, 0.10$ (syst) pb a dává faktor přežití $S^{\text{excl}}_{p_{T,ll}} = 0.883 \pm 0.020$ (stat).

Klíčová slova: ekluzivní photonem-indukové procesy, produkce dileptonů, produkce dibosonů, ATLAS experiment

Acknowledgement

My deepest gratitudes go to my supervisor Oldřich Kepka for his guidance throughout the last three years. I could not imagine learning and achieving so much in such a short time. I would also like to thank Mateusz Dyndal, from whom I learned a lot during our collaboration on the dilepton analysis. Last but not least, I am grateful to my family for their support during my studies.

Contents

List of Figures

Introduction

Photons and their interactions are important part of our everyday lives. We encounter them in many forms, including the visible light or the electromagnetic interaction. On energy scales we most commonly experience, orders of MeV and lower, photons interact only with charged particles. Whether it is the photoelectric effect or pair production, an interaction with another photon is not present. Nevertheless, when we move to higher energies, as e.g. at the LHC at CERN, we can observe such processes. It is of course not a direct interaction since photons do not carry an electric charge, but it is instead mediated by a charged propagator. One example of such process is shown in Figure 1, where the propagator is a lepton and two leptons of the same flavour can be observed in the final state.

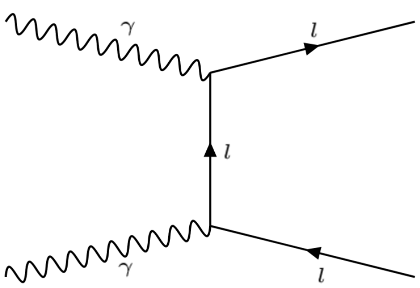

Figure 1: Feynman diagram of exclusive dilepton production.

However, the LHC does not collide high-energy photons, but protons. Due to relativistic contractions, the interacting protons have a significantly deformed electromagnetic field. The transverse component of such field can be interpreted as a quasi-real photon - a photon with a low value of virtuality $Q^2 = |P_\gamma^2|$. A theory describing collisions of such photons is called Equivalent Photon Approximation (EPA) and it allows us to study photon-induced processes in collisions of protons. Due to their lower cross-section in comparison to strong processes, they are often obscured by a significant background and carefully thought-out selection has to be implemented.

Another complication is that the pure QED cross-section of photon-induced processes is reduced due to additional interactions between the colliding protons. This is not to say that the cross-section predicted by the Standard Model is wrong, but that exclusive (purely QED) production is lower due to these accompanying strong processes. The difference between the theoretical σ^{EPA} and the measured cross-section $\sigma^{\mathrm{measured}}$ is quantified by a survival factor S :

$$\sigma^{\mathrm{measured}} = S \cdot \sigma^{\mathrm{EPA}}. \tag{1}$$

Measurement of the survival factor is usually performed as a part of analysis of photon-induced dilepton production. It has the biggest yield from the diphoton processes aside from production of two quarks. Dilepton production also contains only two particles in the final state, unlike the diquark channel where hadronization and other QCD processes lead to large particle multiplicity. It is therefore easier to identify and it also has a precise theoretical prediction within the QED. For these reasons it is the ideal channel to study the survival factor and hence serves as a standard candle of the photon physics at the LHC.

Studies of this factor was done at 7 TeV with both ATLAS and CMS experiment and they will be summarized later. This measurement was repeated at 13 TeV and will be also briefly introduced, with emphasis on my contribution to the analysis. Aside from new energies, a dependency of the factor on several kinematic variables can be studied due to larger data statistics.

With survival factor at our disposal, one can have a look into another processes. One of them is a production of two W bosons, which still has sufficient yield to be properly measured and therefore can be used as a test of the Standard Model. On the other hand, due to presence of the quartic vertex (see Figure 2) it is also a measurement sensitive to presence of an anomalous coupling and as such can be used as a probe of the beyond Standard Model (BSM) physics. An anomalous coupling can be also studied in a triple gauge coupling, which also contributes to the diboson production, but there are another non-exclusive processes more sensitive to it.

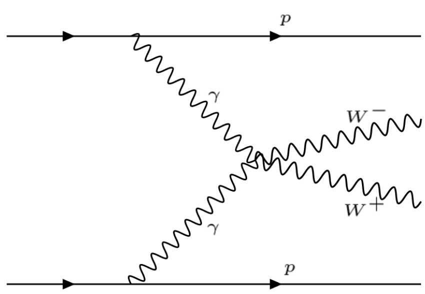

Figure 2: Feynman diagram of exclusive WW production in quartic gauge coupling channel in proton-proton collision.

In comparison to the pure dilepton production, measurement of the diboson final state has a significantly lower yield. Analysis done with the ATLAS detector at 8 TeV observed only around 23 events, compared to thousands of exclusive dilepton events. Thanks to several factors, which will be discussed later, yield at 13 TeV is improved. It will eventually lead to stricter limins on new BSM processes. In this thesis, the preliminary result of the exclusive WW SM cross-section is presented. The full analysis chain has been completed, which is important milestone towards publication of the results.

Chapter 1

Theoretical overview

1.1 The Standard model

The Standard Model of physics is a modern theory describing forces and particles found in nature. It describes three of the four fundamental forces - strong, weak and electromagnetic. Only the gravitational force is not implemented; however, this deficiency does not concern us since gravity has negligible effect on the physics at the LHC.

The Standard Model represents our best understanding of physics of the elementary particles, but it is known to be incomplete. For example, it does not explain the phenomena of neutrino mass or the dark matter. There are many theories trying to explain those problems, e.g. Supersymmetry, but none of those have been experimentally confirmed.

1.1.1 Particles of the Standard model

The elementary particles of the Standard Model are divided between fermions with a half-integer spin and bosons with an integer spin. The elementary fermions are further split into two groups - quarks and leptons [1]:

Quarks are particles which build-up hadrons, e.g. protons and neutrons. They are divided into three generations and have charge either +2/3 (up, strange and top quarks) or -1/3 (down, charm and beauty quarks), with corresponding antiparticle partners. The up and down quarks are the lightest and are generally stable, unlike the heavier quarks which decay through the weak interaction. Quarks are the only elementary particles which interact through all three forces.

Leptons also have three generations, each consisting of a charged and massive particle (electron e, muon μ and tauon τ) and its corresponding neutrino, which is neutral and in Standard Model assumed to be massless[1]. The former interacts through the weak and the electromagnetic interaction while the latter only through the weak one. Again, only the lightest electron ($m_e = 511$ keV) is stable, while the two heavier leptons ($m_\mu = 106$ MeV and $m_\tau = 1777$ MeV) decay.

The elementary gauge bosons are carriers of the three forces:

Photon carries the electromagnetic force. It has no mass, spin 1 and does not have a charge. Those properties result in a long-range effect of the force.

Gluons are responsible for the strong interaction. They carry the colour charge and can therefore self-interact. They are also massless, but due to the self-interaction the force

[1]The Standard Model is known to be incomplete. Presence of neutrino oscillations provides a strong evidence for massive neutrinos. Their mass, which is currently known to be smaller then $\approx$ eV, is of no consequence to this analysis.

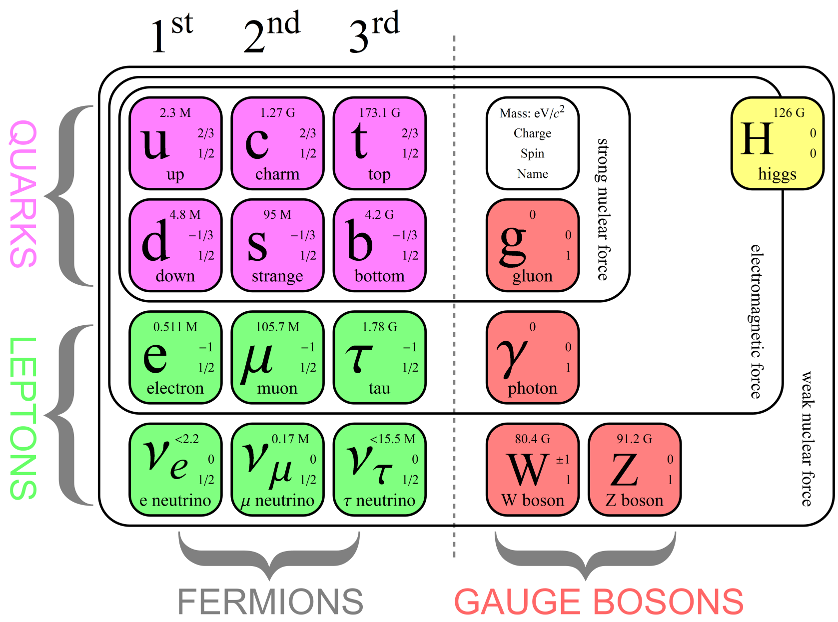

Figure 1.1: Particles of the Standard Model, divided based on their categories and type of force they interact through. Taken from [4].

is short-ranged.

Weak bosons are divided between one charged boson W^+ with its corresponding anti-particle W^- and one neutral boson Z. They carry the weak force and unlike the photons or gluons, they are massive. With $m_W = 80.4$ GeV and $m_Z = 91.2$ GeV they are one of the heaviest elementary particles, leading to a short range of the weak force.

Finally, the **Higgs boson** is a particle responsible for the mass of elementary particles. It interacts with all massive particles, where in the Standard Model this excludes only neutrinos, gluons and photons.

All the elementary particles are summarized in Figure 1.1.

1.1.2 Quantum electrodynamics

Quantum electrodynamics (QED) is a quantum field theory of electromagnetic interaction. It has an infinite range and is propagated by a massless photon. The interaction of particles via QED can be derived using Lagrangian:

$$\mathcal{L}_{QED} = \bar{\Psi}(i\gamma^\mu \partial_\mu - m)\Psi - \frac{1}{4} q_e \bar{\Psi}\gamma^\mu \Psi A_\mu - \frac{1}{4} F^{\mu\nu} F_{\mu\nu},$$

where Ψ and A^μ describe fields of fermion and photon. The first term is a kinematic term of a free 1/2-spin particle, the second term describes an interaction of a fermion with a photon and the last term is a free electromagnetic field, with $F^{\mu\nu} = \partial^\mu A^\nu - \partial^\nu A^\mu$. It is important to note that there is no self interaction between photons in the QED.

A strength of an interaction is connected with a value of a coupling constant α. In processes we experience in everyday life, the constant has value $\alpha_{em} = e^2/4\pi = 1/137$. Although it is called a constant, its value depends on the scale of the given process. The

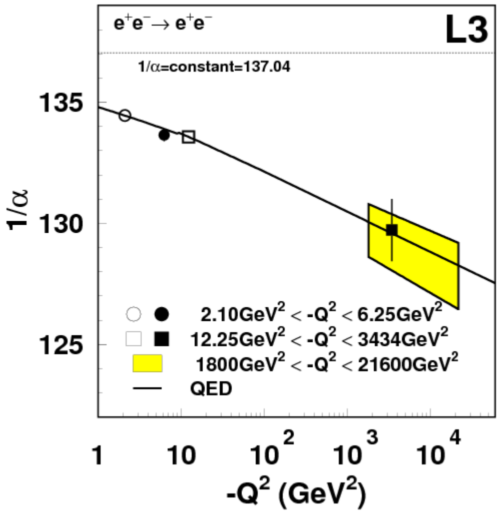

Figure 1.2: Comparison of predicted dependence of QED coupling constant on scale $-Q^2$ and data acquired by LEP. Taken from [5].

dependence on virtuality[2] Q^2 is following:

$$\alpha_{em}(Q^2) = \frac{\alpha_{em}(m_e)}{1 - \Delta\alpha_{em}(Q^2)} \approx \frac{\alpha_{em}(m_e)}{1 - \frac{\alpha_{em}(m_e)}{3\pi}\log(\frac{Q^2}{m_e^2})}$$

in the first order of a perturbation theory. It diverges for $Q^2 \to \infty$. The dependence is caused by a sea of virtual particles (primarily electron-positron pairs) surrounding the charged particle, effectively screening its charge. Higher the transferred momentum, the closer to the charge we are and smaller the screening is.

The scale dependence of the Quantum Electrodynamics was tested for example on the LEP experiment at CERN. The theory and data show an excellent agreement [5]. The results are in Figure 1.2.

1.1.3 Electroweak theory

The weak force is the weakest of the forces of the Standard Model. It is also the only force concerning all the elementary particles. It was first introduced as an explanation of β decay by E. Fermi, but soon it was found it had a more significant role. The original Fermi Lagrangian had the following form:

$$\mathcal{L}_F = G_f \bar{\Psi}_e \Psi_\nu \bar{\Psi}_p \Psi_n,$$

where $\Psi_e, \Psi_\nu, \Psi_p, \Psi_n$ are electron, neutrino, proton and neutron fields. Original Fermi theory was later expanded with parity violation and additional interactions. However, due to unitarity violation the theory was non-renormalizable and another approach was needed.

Instead of direct interaction of the particles in the β decay, a vector boson was introduced as a propagating particle. Later, it was found that the weak interaction could be

[2]Virtuality is an absolute value of four-momentum P of particle squared: $Q^2 = |P^2|$. More off-shell this value is, more virtual given particle is. It can be either time-like virtuality for $P^2 > m^2 \approx 0$ or space-like for $P^2 < m^2 \approx 0$.

united with the electromagnetic force in an electroweak theory. It is known as *Glashow-Salam-Weinberg* model with $SU(2) \otimes U(1)$ local symmetry[3].

The theory works with one boson triplet $W^{(1)}, W^{(2)}, W^{(3)}$ and one iso-scalar boson B_μ. Photon A and new neutral boson Z are connected with wave-functions of the original fields through Weinberg angle Θ_W:

$$Z = W^{(3)} \cos\Theta_W - B \sin\Theta_W, A = W^{(3)} \cos\Theta_W + B \sin\Theta_W,$$

while charged bosons W are linear combinations of the $W^{(1)}, W^{(2)}$:

$$W^+ = \frac{W^{(1)} - iW^{(2)}}{\sqrt{2}}, W^- = \frac{W^{(1)} + iW^{(2)}}{\sqrt{2}}.$$

The Weinberg angle also connects the mass of Z and W bosons: $M_Z^2 = M_W^2 / \cos^2\Theta_W$.

In the original theory the Lagrangian does not have mass term for the weak bosons, otherwise the theory would violate the local symmetry. Also, it violates the unitary e.g. in WW scattering. By a process of spontaneous symmetry breaking through a scalar Higgs boson the triplet of bosons gains mass. The theory is still renormalizable and additional interactions with the Higgs boson cancel remaining divergences when boson momenta go to infinity. Higgs discovery came in 2012, around 50 years after its prediction, marking a huge success of the Standard Model and the LHC [7, 8].

1.1.4 Quantum Chromodynamics

The final piece of the Standard Model puzzle is the Quantum Chromodynamics (QCD). Its origins are connected to the force binding nucleons in nuclei, but as was the case with the other forces, it had proven to be much more complicated.

The Quantum Chromodynamics describes interactions between quarks and gluons - particles carrying colour charge. That can be compared to electromagnetic charge, with the main difference being that instead of simply having a positive and a negative charge, the QCD has red and anti-red ($R\bar{R}$), green and anti-green ($G\bar{G}$), and blue and anti-blue ($B\bar{B}$) charges. The QCD is built on SU(3) group symmetry with three generators, each connected to one of the colours.

Gluons, the propagators of the strong force, carry a combination of colour and anti-colour (e.g. $B\bar{G}$), where the combinations can be described by an octuplet. This leads to, in contrast to the QED, a self-interaction and thus to drastically different properties of the force.

The main difference between QCD and QED is connected to the running constant of the strong interaction α_s, where its value rises with decreasing value of Q^2, as can be seen in Figure 1.3. This means coloured objects are strongly attracted at higher distances. For this reason, the coloured particles are confined in a colour singlet and on macroscopic scales colour cannot be observed. This property of the strong force is called confinement.

On the other hand, at higher energies the force is minimal and the particles move as if they were free, hence this behaviour is called asymptotic freedom.

1.2 Photon-photon interactions

There are many processes allowed by the Standard Model. One category of processes, studied in this thesis, is photon-induced production - a photon-photon interaction giving

[3] SU(2): Unitary 2x2 matrices with determinant equal to 1, U(1) Unitary 1x1 matrices.

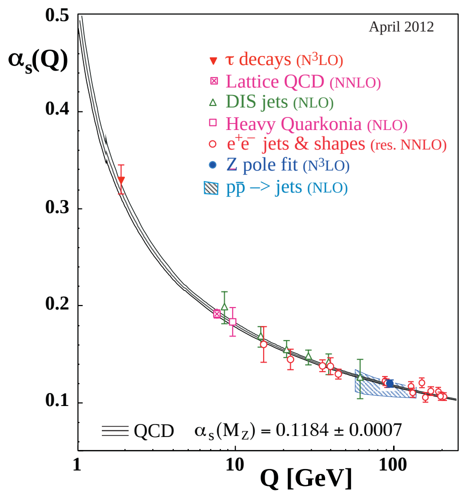

Figure 1.3: Dependence of coupling constant of the strong interaction α_s on Q^2. Taken from [6].

various final states. They are often purely QED or Electroweak processes, which is useful when studying e.g. anomalies in Electroweak coupling mentioned later. The primary goal of their measurement is however Standard Model confirmation. This is important since most of those processes were either never measured, or were first measured rather recently at the LHC.

A possibility of diphoton interactions was proposed in 1934 in a paper by L. D. Landau and E. M. Lifschitz [9]. It described production of an electron-positron pair in photon-photon interactions. The proper theory, however, came much later with the QED and with the Electroweak theory.

Diphoton processes have never been observed in a direct collision of two photons, but they can be measured in collisions of ultra-relativistic charged particles. This will be discussed in more detail in the next chapter. Processes studied at the LHC are summarized in following sections:

1.2.1 Dilepton production

Dilepton production, in case of an electron final state called Breit-Wheeler pair production, is the most common of the photon-induced processes. The Feynman diagram was already presented in Figure 1. In the lowest order of the perturbation theory the cross-section of dilepton production takes form [11]:

$$\sigma^{\gamma\gamma\to l^+l^-} = \frac{4\pi\alpha^2}{s}\left[\left(1+\frac{4m_l^2}{s}-\frac{8m_l^4}{s^2}2\ln\left(\frac{\sqrt{s}}{2m_l}+\sqrt{\frac{s}{4m_l^2}-1}\right)-\left(1+\frac{4m_l^2}{s}\right)\sqrt{1-\frac{4m_l^2}{s}}\right)\right],$$

where m_l is mass of the lepton (electron, muon or tauon). The $\sqrt{s}$ is the mass of the $\gamma\gamma$ system and thanks to the exclusivity it is equal to invariant mass of the lepton pair, which will be denoted m_{ll} (variable which will be often used). The minimal energy of the system is $\sqrt{s} \geq 2m_l$.

It was found [12], that the production of electron-positron pairs from two photons is responsible for cut-off in high energy gamma rays in cosmic rays. The absorption reaches maximum around photon energy 1 TeV. The production also appears in production of electron pairs in gamma ray bursts [13].

1.2.2 W^+W^- production

The exclusive diphoton production of two weak bosons can happen in three channels (see Figure 1.4), two containing triple gauge coupling and one with quartic gauge coupling.

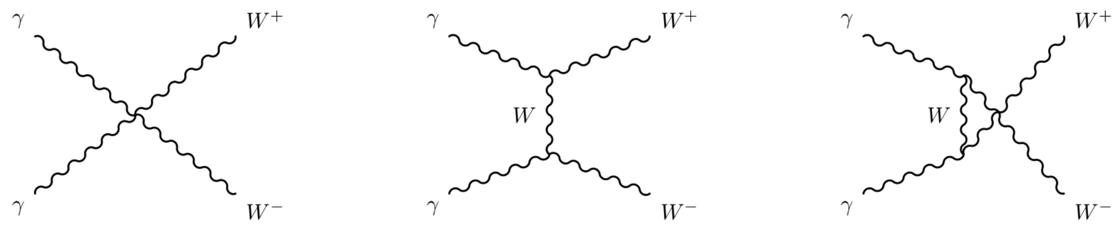

(a) QGC vertex (b) t-channel (c) u-channel

Figure 1.4: Leading channels of the photon-induced W^+W^- production. Taken from [14].

Those processes can be used to study anomalous quadratic gauge coupling (aQGC) and anomalous triple gauge coupling (aTGC) and thus they could be used for investigation of physics beyond the Standard Model. However, until today only aQGC was studied using exclusive WW production, since there are other channels more sensitive to the aTGC.

Using approach described e.g in article [15], one can describe the lowest order of new physics by an introduction of two new coupling parameters $\alpha_0/\Lambda^2, \alpha_0/\Lambda^2$, where Λ is a scale of new physics.

The unpolarized Standard Model cross-section (again in the Born approximation) is [16]:

$$\sigma_{\gamma\gamma\to W^+W^-} = \frac{6\pi\alpha^2}{s}\left[\beta - 4\frac{M_2^2}{s}\left(1-\frac{2M_W^2}{s}\right)\log\left(\frac{1+\beta}{1-\beta}\right)+\left(\frac{1}{3}+\frac{M_W^4}{s^2}\right)\frac{16\beta}{1-\beta^2}\right],$$

where M_W is mass of the W boson and β is a velocity of the W in the center-of-mass system. As was the case for the dilepton production, there is a cut-off at $2m_W$ for the invariant mass of the dilepton system. For high invariant mass of the diphoton system the cross-section becomes constant

$$\sigma_{\gamma\gamma\to W^+W^-} \to \frac{8\pi\alpha^2}{M_W^2} \approx 80\text{pb},$$

and it is a dominant exclusive process at high energies due to the t-channel. Corrections to the first order of perturbation theory are presented in the paper [16].

Analysis of this process is complicated, since the weak bosons quickly decay into additional particles. It is usually measured in a final state containing two leptons.

1.2.3 Light-by-light scattering

Perhaps the most counter-intuitive process is the scattering of a photon off another photon. Since photons do not carry charge and therefore cannot interact directly, this process is only possible through a charged particle propagator. The leading diagram of the $\gamma\gamma$ scattering is a fermion box diagram, displayed in Figure 1.5.

This process had not been observed until very recent measurement by ATLAS. Still, there were limits put on the cross-section. E.g. for 0.8 eV photons it is $\sigma_{\gamma\gamma\to\gamma\gamma} < 1.5\cdot 10^{-24}$ b. For this energy region the predicted cross-section is $7.3 \cdot 10^{-42}$ b [17, 18], so the result is still in an agreement with Standard Model.

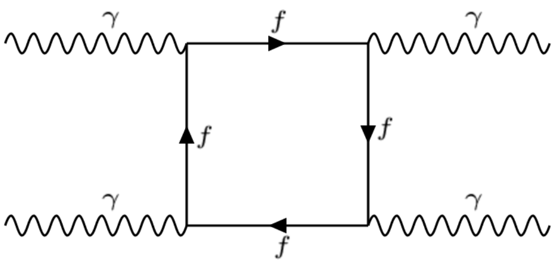

Figure 1.5: Feynman diagram of photon-photon scattering.

Measurement of this process was done with the ATLAS detector in collisions of lead nuclei at $\sqrt{s}$=5.02 TeV. Though it was not yet published, its current state is summarized in conference note [19]. Although the precision of the analysis is low due to low statistic, the measurement shows an agreement with the Standard Model.

1.2.4 Direct $\gamma\gamma \rightarrow e^+e^-$ measurement

Even though there have been many studies of photon-induced processes, there is no measurement of a direct diphoton interaction from collisions of photons. Since the diphoton cross-section increases with an energy, such measurement of direct photon collision would require a high-energy high-intensity photon sources - something not available for a long time. However, in recent years two propositions for such analysis appeared, one combining high energy photons interacting with black body radiation [20] and second for collision of two laser beams [21].

There is, however, an alternative to a direct measurement. As was mentioned in the introduction, relativistic charge particles are accompanied by a field of photons. Interactions of photons can be therefore studied in collisions of such charged particles.

Chapter 2

Photon-induced production in collisions of charged particles

It is technically difficult to realize a photon collider with sufficient energies and intensities to study a photon-photon interaction. However, collisions of charged particles offer a way to study such processes.

For electron collisions, detailed description was first done by C. F. v. Weizäcker and J. Williams [22, 23]. Even though the cross-section of those processes is rather low (mainly due to the presence of numerous photon vertices), it becomes comparable to a cross-section of single photon processes at higher energy [10]. For hadron beams the situation is not so simple since they have a complicated sub-structure, but it is still a powerful tool for an investigation of photon-photon processes.

2.1 The Equivalent Photon Approximation

Due to the relativistic contractions, ultra-relativistic particles have deformed electromagnetic field. Such field can be interpreted as quasi-real photons[1] (this concept is displayed in Figure 2.1). When the particles - whether it is a proton or a nucleus - move past each other, the photon fields can interact while at the same time leaving the colliding particles intact. Those processes are more significant for heavy nuclei, since the intensity of the fields (and therefore of the equivalent photons) is proportional to the charge of the particle.

An interpretation of the transverse field as photons is called *Equivalent photon approximation*, a method first proposed by E. Fermi [25] and further developed by C. F. v. Weizäcker and J. Williams [22, 23]. Given a cross-section of some photon-induced process, e.g. dilepton production $\sigma_{\gamma\gamma\to l^+l^-}(m_{l^+l^-})$, a total cross-section of such process in collision of two protons A_1, A_2 can be written as [29]:

$$\sigma^{EPA}_{A_1A_2\to A_1A_2l^+l^-} = \int\int P(x_1)P(x_2)\sigma_{\gamma\gamma\to l^+l^-}(m_{l^+l^-})\mathrm{d}x_1\mathrm{d}x_2,$$

where x_i are fractions of energy of the proton carried by the photons, P are photon distributions given by the EPA and $m_{l^+l^-}$ is an invariant mass of the dilepton (and at the same time of the diphoton) system. The mass is connected to the x_1, x_2 by simple formula $m^2_{l^+l^-} = x_1x_2s$, assuming there is no crossing angle between the photon trajectories.

Such method can be applied to most of the photon-induced processes, if the virtuality of the photons is small (which can be described by inequality $W_{\gamma\gamma} >> Q^2$) [24]. The

[1] Photons with small virtuality.

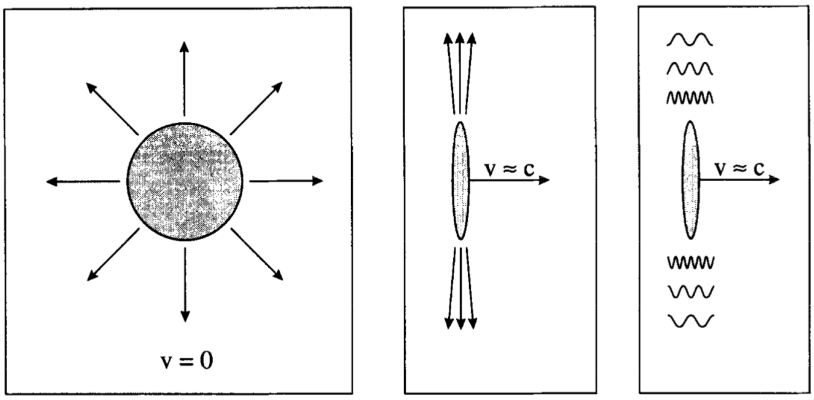

Figure 2.1: Sketch describing Fermi's idea of interpreting EM field of ultra-relativistic charged particles as swarm of photons. Taken from [25].

low virtuality also means that the resulting leptons are emitted back-to-back. For LHC energies the average virtuality of photons is of order 0.01 GeV^2.

For elastic photon collision (where both protons survive the interaction), the photon distribution function can be written as [26]:

$$P_e(x) = \frac{\alpha}{\pi x} \int_{Q^2_{min}}^{Q^2_{max}} \frac{\mathrm{d}Q^2}{Q^2} \left[\left(1 - \frac{Q^2_{min}}{Q^2} \right) (1-x)\, F_E(Q^2) + \frac{x^2/2}{2} F_M(Q^2) \right],$$

where F_E, F_M are electromagnetic structure functions of the proton.

The situation is further complicated by several factors. The electromagnetic field is the strongest in proximity of the proton. However, when the protons are close enough to interact through the strong force, the diphoton production is obscured by additional QCD processes. Furthermore, one or both nuclei may dissociate due to the photon interaction.

All these additional processes complicate the measurement of diphoton production and have to be taken into account.

2.1.1 Impact parameter dependence

The dependence on the impact parameter is connected to the term introduced in the introduction - the survival factor. It takes into account the fact, that aside from the exclusive production, additional proton-proton re-scattering is possible. Even though the diphoton process is still present, it is impossible to distinguish it from other processes due to large number of additional particles.

Given the low transferred momentum, the survival factor is part of the soft QCD (QCD with low momentum transfers) and therefore cannot be computed using the perturbative theory. One of the most recent approaches is summarized in [27] and in more detail in [28]. The basic idea is to parametrize how the amplitude of the process is affected by the additional interaction.

First, consider the amplitude $T(q_{1t}, q_{2t})$ of the bare photon-induced process in Figure 2.2a, where q_{1t}, q_{2t} represent transverse momenta of photons emitted by the protons. The re-scattering amplitude (in Figure 2.2b) can be then defined as $T^{res}(q_{1t}, q_{2t}) = \frac{i}{s} \int \frac{\mathrm{d}^2 k_t}{8\pi^2} T_{el}(k_t^2) T(q_{1t}+k_t, q_{2t}-k_t)$, where $T_{el}(k_t^2)$ represents the additional elastic scattering between the colliding protons with transferred transverse momentum k_t. Combining these

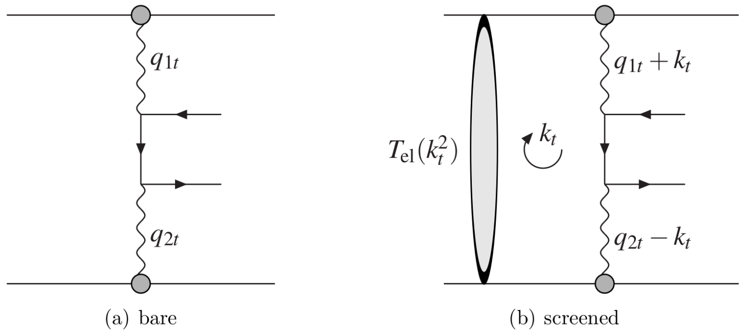

Figure 2.2: Feynman diagrams of dilepton production (a) without and (b) with additional re-scattering of the protons. Taken from [28].

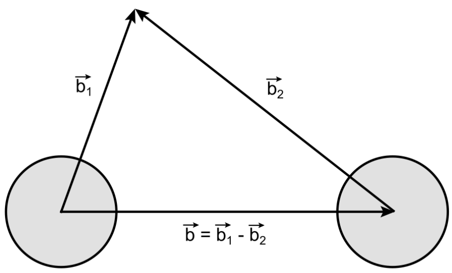

Figure 2.3: Definition of the impact parameter vectors. Taken from [24].

two amplitudes one gets the average survival factor[28]:

$$\langle S^2 \rangle = \frac{\int \mathrm{d}^2 q_{1t} \mathrm{d}^2 q_{2t} |T(q_{1t}, q_{2t}) + T^{res}(q_{1t}, q_{2t})|^2}{\int \mathrm{d}^2 q_{1t} \mathrm{d}^2 q_{2t} |T(q_{1t}, q_{2t})|^2}.$$

This formula can be rewritten in terms of the impact parameters $\vec{b}_{1t}, \vec{b}_{2t}$ describing transverse separation (vectors $\vec{b_1}, \vec{b_2}$ are visualized in Figure 2.3) and distance between the protons $b_T = |\vec{b}_{1t} - \vec{b}_{2t}|$ [27]:

$$\langle S^2 \rangle = \frac{\int \mathrm{d}^2 \vec{b}_{1t} \mathrm{d}^2 \vec{b}_{2t} |T(\vec{b}_{1t}, \vec{b}_{2t})|^2 \exp(-\Omega(s, b_t))}{\int \mathrm{d}^2 \vec{b}_{1t} \mathrm{d}^2 \vec{b}_{2t} |T(\vec{b}_{1t}, \vec{b}_{2t})|^2},$$

where $\Omega(s, b_t)$ is a proton opacity and $\exp(-\Omega(s, b_t))$ describes the probability of no inelastic scattering at impact parameter b_t. It is measured in elastic collisions of protons. The suppression of the exclusive production is bigger with smaller distance between the protons - behaviour one would expect.

In reality, one cannot measure the impact factor, but it is still manifested in the dependence of the survival factor on other variables. Study of those dependencies (aside from the measurement of the average survival factor) is one of the motivations for the dilepton measurement at 13 TeV.

2.1.2 Dissociative production

Even though the momentum transfers are usually small and protons emitting the photons are deflected at small angles, they can sometimes dissociate into additional partons, as

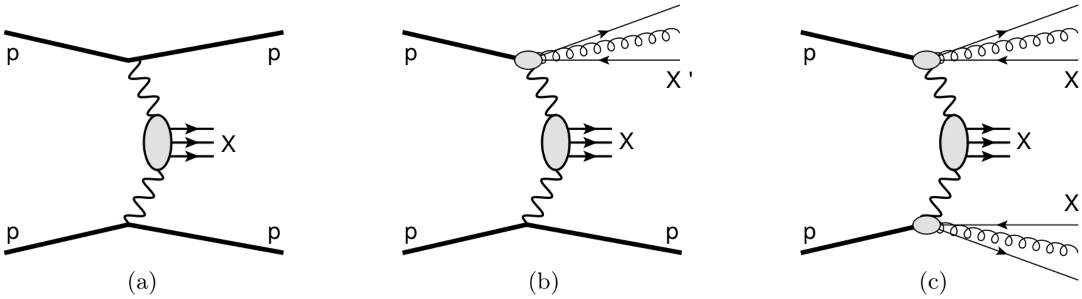

Figure 2.4: Diagrams showing the three basic types of diphoton production: (a) elastic, (b) single dissociative and (c) double dissociative. Taken from [24].

shown in Figure 2.4, where either one or both protons break down. Thus, we have three possible reactions: *exclusive* (or elastic), where both protons survive, *single dissociative* (SDiss), where one of the protons survives and finally *double dissociative* (DDiss) with both protons destroyed.

Since the dissociation involves QCD effects, its computation is more complicated. It affects the final state leptons and therefore the dilepton spectra are significantly different from those in the elastic case [30]. The dissociative component is often indistinguishable from the elastic production, since the partons from the dissociation are usually emitted in a forward direction and are often not detected.

2.2 Previous measurements of the dilepton production

The exclusive dilepton production was already studied by several experiments, e.g. at the Tevatron for both electrons and muons with the CDF experiment [31, 32, 33], at HERA with the H1 detector [34] or at the RHIC with experiments STAR [35] and PHENIX [36]. All analyses were in agreement with the Standard Model.

The survival factor was studied by ATLAS [29] and CMS [30] experiments at the LHC. Both measurements were performed at the 7 TeV in proton-proton collisions for muons, ATLAS also included the production of electron-positron pairs.

Both analyses used a similar method to derive the survival factor and arrived to compatible results, which are displayed in Figure 2.5. The survival factor was found to be around 80%. Presented 13 TeV measurement was inspired by the ATLAS analysis. Due to the better statistics during Run 2 at the LHC, much more precise results are obtained, which allows us to study a dependence of the survival factor on various kinematic observables.

2.3 Previous measurements of the diboson production

Measurement of the diboson final state was first performed by the CMS experiment at 7 TeV [38], followed by 8 TeV analysis by both ATLAS [37] and CMS [39]. Similar in approach, both experiments sought confirmation of the Standard Model and possible search for new physics in anomalous quartic gauge coupling mentioned earlier in Section 1.2.2.

The limits of the coupling constants $\alpha_c/\Lambda^2, \alpha_0/\Lambda^2$ measured by both LHC experiments

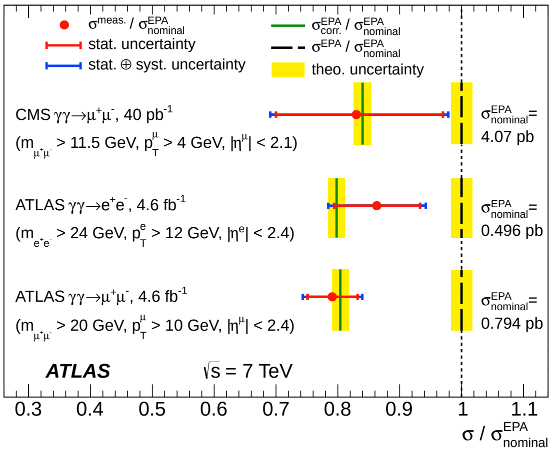

Figure 2.5: Survival factors derived in ATLAS and CMS for the dilepton production, compared to theoretical prediction. Taken from [29].

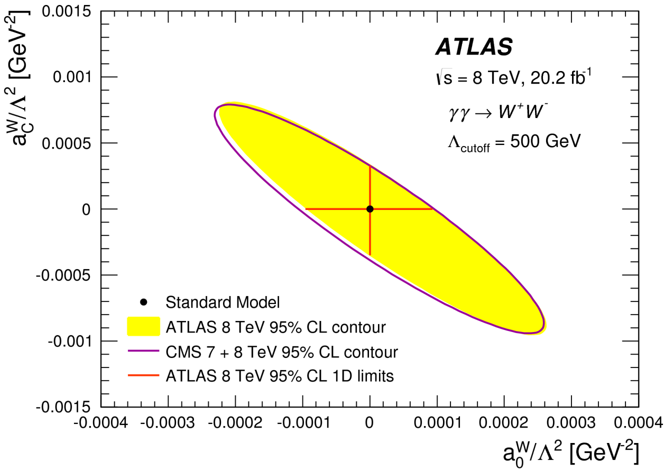

Figure 2.6: Measured limits on coupling parameters $\alpha_c/\Lambda^2, \alpha_0/\Lambda^2$ of an anomalous quartic gauge coupling by the ATLAS and CMS experiments. Taken from [37].

can be found in Figure 2.6. Both results are compatible with the Standard Model within the uncertainties and do not offer any evidence of new physics.

Chapter 3

Experiment ATLAS

The measurement described in this thesis was performed utilizing data provided by the ATLAS experiment located at the Large Hadron Collider. Both the accelerator and the detector are described in this chapter, focusing on instrumentation relevant to the analysis.

3.1 The Large Hadron Collider

Located in the CERN laboratory near Geneva, the Large Hadron Collider (LHC) is the largest proton-proton synchrotron in the world. In order to mitigate the abundant cosmic radiation, it is located 60-140 meters underground. Bunches of protons are accelerated in opposite directions in two separate beam pipes up to staggering $\sqrt{s}$ =13 TeV center-of-mass energy[1].

The protons are kept on 27-kilometre long semi-circular orbit using 1232 large superconducting magnets with magnetic field strength circa 8 Tesla. The superconductivity is maintained using liquid helium cooled down to 1.9 K, a temperature lower than that in the outer space [40].

In order to minimize the loss of protons in the accelerator, a high vacuum needs to be maintained in the beam tubes. The pressure in the tubes is 10^{13} times lower than that of the atmosphere. There are two other layers of vacuum around the beam pipes used to isolate the superconducting magnets and the helium distribution.

3.1.1 Accelerator complex

The life of an LHC proton does not start at the collider, but much sooner. A whole accelerator complex, starting at simple hydrogen bottle, is used to accelerate the particles up to LHC injecting energy - a 450 GeV per proton. First, the hydrogen atoms are ionized and then speed up using *LINAC 2* accelerator up to 50 MeV.

The *LINAC 2* is followed by the Proton Synchrotron Booster (PSB) and Proton Synchrotron (PS), which further accelerate the protons up to 1.4 GeV or 25 GeV respectively. The last pre-accelerator is the Super Proton Synchrotron, which brings the particles up to the injecting speed. Filling up of the LHC takes around 4 minutes, with additional 20 minutes are needed to accelerate the particles to their maximal energy.

Aside from protons, lead ions are also used in collisions at the LHC and that either in both beam pipes or in proton-lead configuration. The analysis presented in this thesis, however, only considers proton collision.

[1]Current value, the maximal designed energy is $\sqrt{s} = 14$ TeV.

The LHC pre-accelerators are part of a bigger complex used to supply particles to the vast number of experiments performed at CERN.

3.1.2 LHC experiments

The protons at the LHC are divided into two beams which circulate in two separate tubes in opposite directions. There are four interaction points, where the beams are allowed to cross and interact. This is where the four main LHC experiments are located. They detect particles from the collisions and use this information to perform physics measurements.

Two of them, which are the most relevant for this measurement, are the ATLAS and the CMS experiments. They are general purpose detectors, designed for Standard Model measurements and searches for new physics. They are responsible for the Higgs boson discovery in 2012 and besides that for many Standard Model measurements and beyond Standard Model searches.

The third experiment, ALICE, focuses mostly on collisions of ions. Specifically, it studies the quark-gluon plasma. The last detector is the LHCb. As the name suggest, the LHCb focuses on b-physics and studies the CP violation.

3.1.3 Luminosity

As was mentioned earlier, the purpose of an accelerator is to supply the detectors with collisions. In simplified point of view, larger the number of collision per unit time the better the performance, since the experiments collect more data and can access rare processes. A rate of a process R is proportional to its cross-section σ and luminosity L:

$$R = L\sigma$$

Luminosity is where the performance of the accelerator comes in, since it depends on the beam parameters. Narrower the beam and higher the frequency with which the bunches of protons collide, higher the obtained luminosity.

The planned maximal luminosity of the Large Hadron Collider is $L = 10^{34}\text{cm}^2\text{s}^{-1}$, but as can be seen in Figure 3.1a, which displays the peak luminosity during the year 2016, the LHC has already outperformed its design approximately 1.4 times.

In this thesis two data samples are considered. For measurement of photon-induced diboson production data from 2016 with $\sqrt{s} = 13$ TeV are used. The total delivered luminosity from this year and amount of it which was recorded by the ATLAS is displayed in Figure3.1b. Excluding incomplete and corrupted events, this lead to total integrated luminosity $L_{tot} = 33.3$ fb^{-1} good for data analysis. Second data-taking period, used in analysis of dilepton final state, was recorded during 2015 with total luminosity 3.19 fb^{-1}.

Luminosity at the LHC is measured using a van der Meer scan technique, proposed by S. van der Meer in 1968 [41]. It is based on measurement of particle production as a function of the impact parameter between the two colliding beams. More details regarding the implementation can be found in note [42].

Though bigger luminosity leads to greater production of particles, it is not purely advantageous. With higher luminosity more protons collide per each bunch crossing, meaning that aside from process one wants to study a significant background is always present. This especially affects exclusive analyses, since they are based mainly on separation of the photon-induced processes from other particle activity.

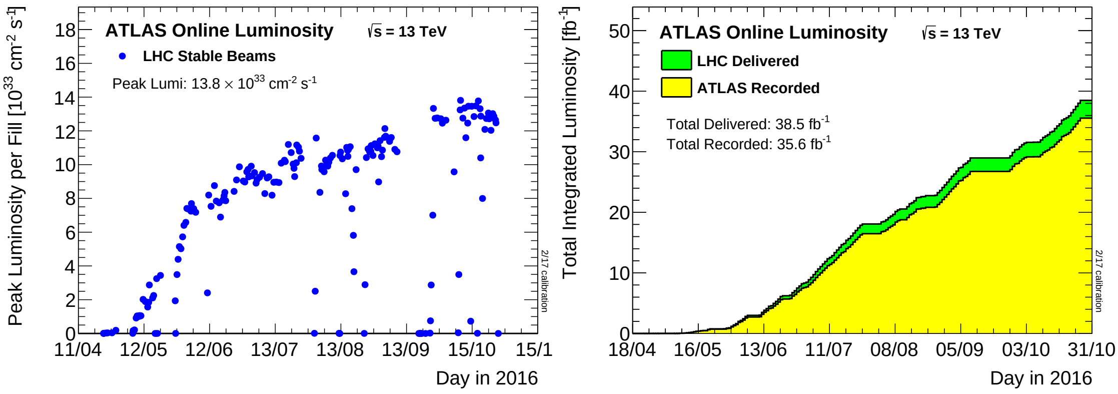

(a) (b)

Figure 3.1: (a) Peak luminosity per fill throughout the 2016 data-taking. (b) Integrated luminosity delivered by the LHC and luminosity recorded by the ATLAS experiment in 2016, taken from [44].

3.2 The ATLAS detector

A Toroidal LHC Apparatus (ATLAS) is a general purpose detector. This means it is designed to reconstruct as wide variety of events as possible. Hence, it needs to cover as large phase-space around the interaction point as possible. The detector is symmetrical around the beam pipe, with 25 meters in diameter and 46 meters in length. It has variety of subdetectors, which can be divided into four categories: Inner Detector, Electromagnetic Calorimeter, Hadronic Calorimeter and Muon spectrometer, each focusing on reconstruction of some specific group of particles.

Aside from the detector elements, there is a complex structure of magnets, which bend trajectories of electrically charged particles. This makes it possible to assess their momentum. The magnet system is divided into three parts: the first is a 2T solenoid superconducting magnet placed around the Inner Detector. The second one encapsulates the Muon Spectrometer and is a 0.5 T toroidal magnet. Finally, there is a 1T magnet in the end-caps behind the Inner Detector. The whole ATLAS with all its main parts is displayed in Figure 3.2.

3.2.1 ATLAS coordinate system

Before delving into details of the ATLAS subdetectors, it is necessary to define a coordinate system and main variables used by the ATLAS. The origin point is located in the centre of the detector. The y axis points upward, the x points towards the centre of the LHC ring and the z axis goes along the beam pipe. Since most of the particles are emitted from a single point, a spherical system is sometimes more appropriate, with ϕ being an angle in xy plane, while θ is an angle from the z axis to this plane.

Another coordinate is the *pseudorapidity* η defined as $\eta = -\log\tan\frac{\theta}{2}$, which is useful since a) particle production is nearly flat as function of pseudorapidity and b) in limit of zero masses it is equal to *rapidity* $y = \frac{1}{2}\log\frac{E+p_z c}{E-p_z c}$, which is additive under Lorentz transformation along the beam pipe.

Distance in ϕ, η plane $R = \sqrt{\Delta\phi^2 + \Delta\eta^2}$ is useful in e.g. reconstruction and matching of objects. Finally, a component of momentum perpendicular to the z axis p_{T}, called transverse momentum, is also often used. It is easily determined from a curvature in the

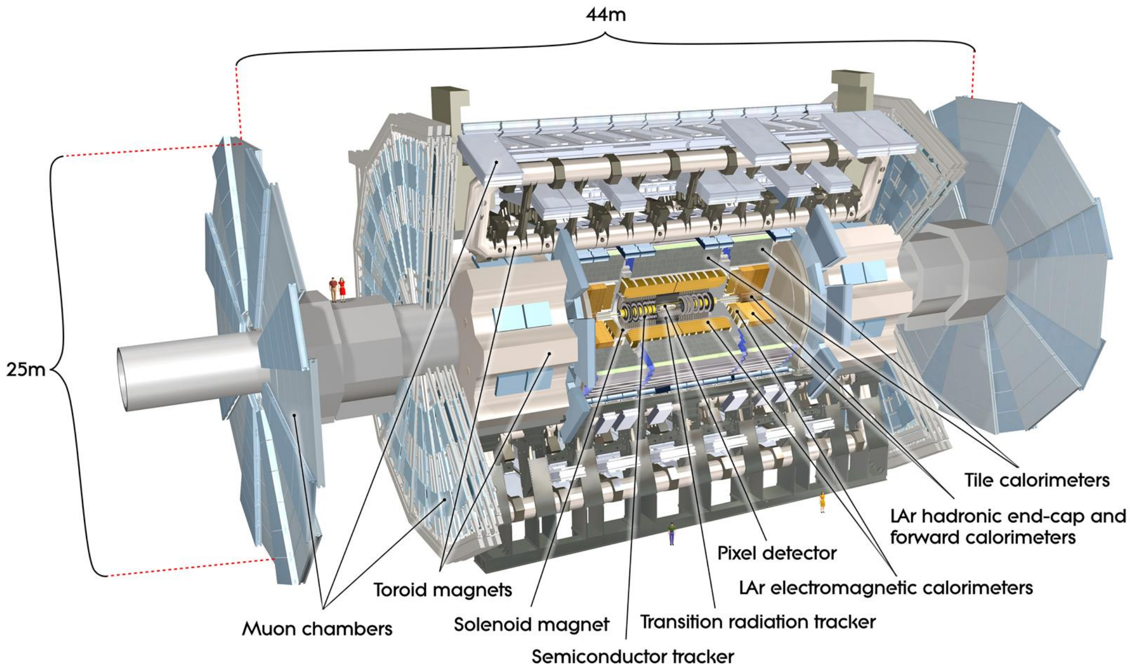

Figure 3.2: Overview of main parts of the ATLAS - Inner Detector, Hadronic and Electromagnetic Calorimeters and Muon Detector, taken from [43].

solenoid field in the Inner Detector and also is invariant under a Lorentz transformation parallel with the beam pipe.

3.2.2 ATLAS triggers

The ATLAS computing would not be able to process and save all the collisions due to the high rate of events. In order to reduce the rate, numerous triggers are implemented. They are set up in such way, that they focus on interesting events. One example can be the `HLT_2mu6` trigger (used later in this analysis), which fires when there are two muons with $p_T > 6$ GeV detected. The triggers are often pre-scaled, meaning only every n-th event is saved, in order to further reduce the event rate.

First level of the trigger is a part of the detector hardware. It reduces the maximal 40 MHz collision rate of events to only 75 kHz. It searches e.g. for high p_T leptons, jets or large missing energy. To reduce the event yield further, a High-Level Trigger (HLT) is employed, which reduces the trigger rate to a frequency around 1 kHz. For example, this thesis uses several HLT triggers which search for lepton with various flavours and transverse momentum, but those will be discussed in more detail later.

3.3 Inner detector

The Inner Detector is responsible for a reconstruction of trajectories of charged particles (from now on called simply tracks). Point at which collision or decay took place and from which tracks usually originate is called vertex. It is another object reconstructed using the inner detector.

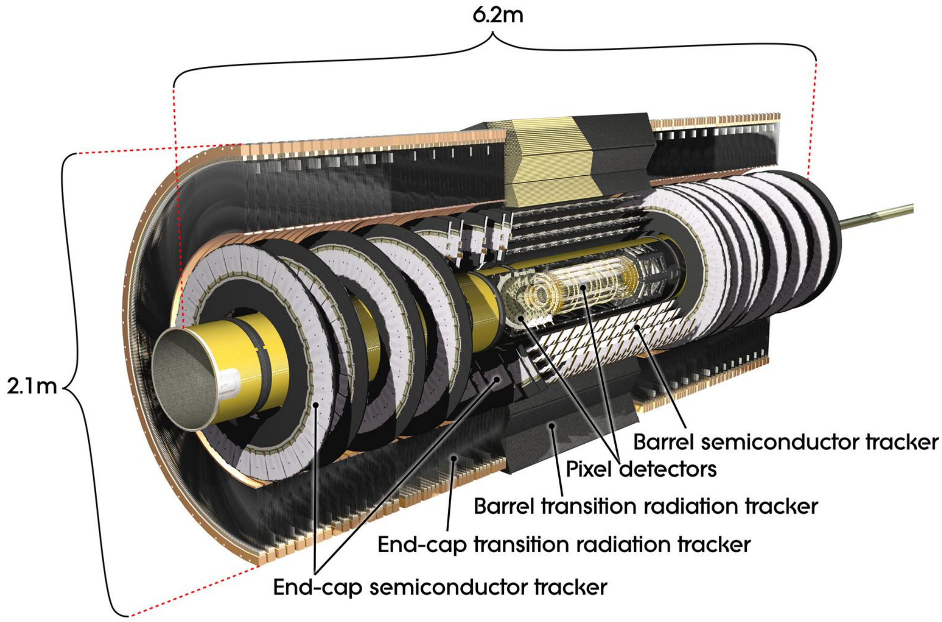

Figure 3.3: Overview of the Inner Detector - barrel and end-cap, consisting of Pixel, SCT and TRT subdetectors, copyright by **ATLAS Experiment ©2014 CERN**.

The ID has three subdetectors (Pixel, SCT and TRT) in different distances from the beam pipe, which is reflected in their properties. Closer to the beam pipe, where activity is high, the detector needs to have a better granularity, while the outer layers have a larger area to cover. All three layers are divided into a barrel and two end-caps.

As was mentioned earlier, it is possible to determine the transverse momentum from trajectories of particles. These trajectories follow a helix. Radius of the helix is proportional to their transverse momentum. Thus, at high momenta the radius is so large the tracks are practically linear, leading to worse p_{T} resolution. On the other hand, when the p_{T} is too low, the particle does not reach enough layers of the detector to be properly reconstructed. The lowest possible value of p_{T} reconstructed at the ATLAS is around 100 MeV. However, contribution of pile-up tracks at low momentum is too large and the minimal value used is set to 400 MeV. As for the spatial coverage of the detector, it detects particles in the full ϕ angle and up to $|\eta| = 2.5$ in pseudorapidity.

It is useful to determine the distance of a track to e.g. vertex from which it originated. This distance is derived from the point of the closest approach of the trajectory to the vertex and in ideal case it would be zero, but since both tracks and vertices have finite resolution, it is not really the case. Two parameters are often used. In the xy plane, the transverse distance is d_0. The longitudinal distance from the vertex is labelled z_0 , which is a distance along the z axis. Illustrations of the impact parameters and of the transverse momentum are in Figure 3.4a.

In the case of the tracks, the resolution in the z is worse the more forward they are. In order to account for this, a $z_0 \sin\theta$ is often used instead for selection. Distribution of the tracks for this variable is displayed in Figure 3.4b and as can be seen, most of the tracks are focused in 1 mm region within the interaction.

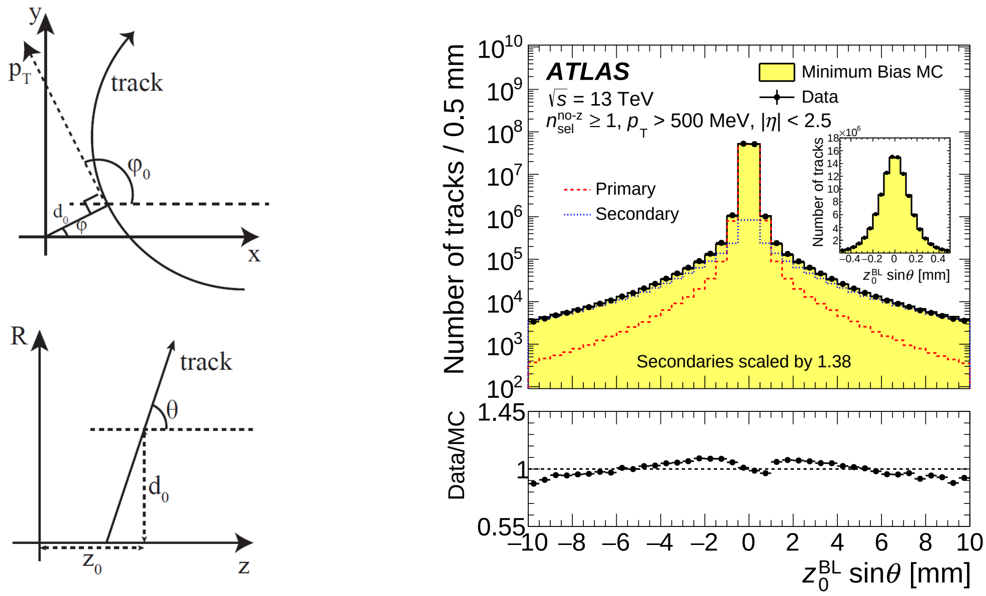

(a) (b)

Figure 3.4: a) Distribution of tracks as a function of the longitudinal impact parameter $z_0^{BL} \sin\theta$ [46]. b) Definition of transverse d_0 and longitudinal z_0 impact parameter and transverse momentum p_{T}, taken from [47].

3.3.1 Pixel detector

The innermost detector of the ATLAS is the Pixel detector. Since it is in a region with high particle density, it needs to have a really good granularity. It was upgraded during the first long LHC shut-down. The original design is discussed first, followed by a description of the upgrade.

The Pixel detector is composed of three layers in both the end-caps and the barrel. Its 1.7m^2 surface is covered by 1744 identical sensors each with 47233 pixels. Thanks to the large number of pixels it has resolution of 10-100 μm [48]. This leads to approximately 80 millions readout channels, 90% of all the channels in the ATLAS [24].

The Insertable B-Layer (IBL) was added to the Inner Detector in order to help with the increased pile-up expected during the Run 2. A good performance of reconstruction of the tracks is achieved by using pixels with a smaller size than those in the rest of the Pixel detector. The IBL is an additional layer of the Pixel Detector placed closest to the beam. The original beam pipe had to be replaced by one with a smaller radius in order to make a place for the new layer [24].

3.3.2 SCT detector

The Semi Conductor Tracker (SCT), a silicon strip detector, is placed around the Pixel detector. The barrel part has four layers and covers $|\eta| < 1.4$. On the other hand, each end-cap has nine layers and covers $1.4 < |\eta| < 2.5$. There are in total 15912 silicon sensors, each 12 cm long and 80 μm wide [24].

Since the SCT is a strip detector, each sensor can provide only a 2D information about the passing particle. To reconstruct the point of passage (a hit) completely, the SCT is made of two back-to-back layers, with a small angle between the strips ($\approx 10°$). The narrow angle has a smaller resolution in comparison to e.g. perpendicular configuration,

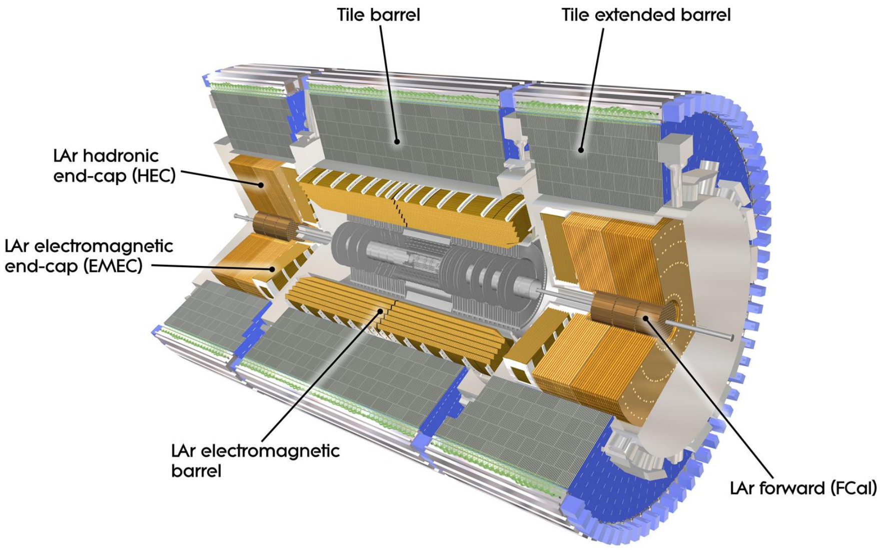

Figure 3.5: Schematic of the ATLAS calorimeter system, taken from [45].

but significantly reduces the contribution of ghost hits - a hit obtained by the combination of signals from two strips which were however fired by different particles.

3.3.3 TRT detector

The outermost detector of the ID, the Transition Radiation Tracker (TRT), covers ś$|\eta| < 2$, with a division between the barrel and end-caps at $|\eta| = 1$. It is composed of straws filled with a gas and thin wire in its centre. Passing particle ionizes the gas, creating a current. Based on the drift time, a more precise point of passage can be measured.

Aside from simple hit detection, the TRT is used to separate electrons from e.g. charged pions. The straws are surrounded by a radiative material. Particles passing through this material emit a transition radiation, which is then detected by the straws. This emission is much larger for the electron, which can be used for their identification.

3.4 Calorimeters

Calorimeter is an experimental technique used to measure energy of particles. When a particle transverses a dense material it loses energy through a shower until it is stopped. The calorimeter then measures the energy deposited by the shower. They usually have an absorber part, which stops the particle and produces the shower, and a sampling material, which measures the signal. The ATLAS calorimeter system is displayed in Figure 3.5. All information is taken from [45].

Electromagnetic calorimeter - the main goal is to measure and identify electrons and photons. It has a lead absorber and a liquid argon for sampling. It covers the whole ϕ region and is composed of a barrel and two end-caps with total coverage $|\eta| < 3.2$. The barrel is divided into two parts with a small gap at $z = 0$. The detector has an accordion geometry, which provides a full ϕ coverage.

In order to ensure that most of the energy is contained within the EM calorimeter, its

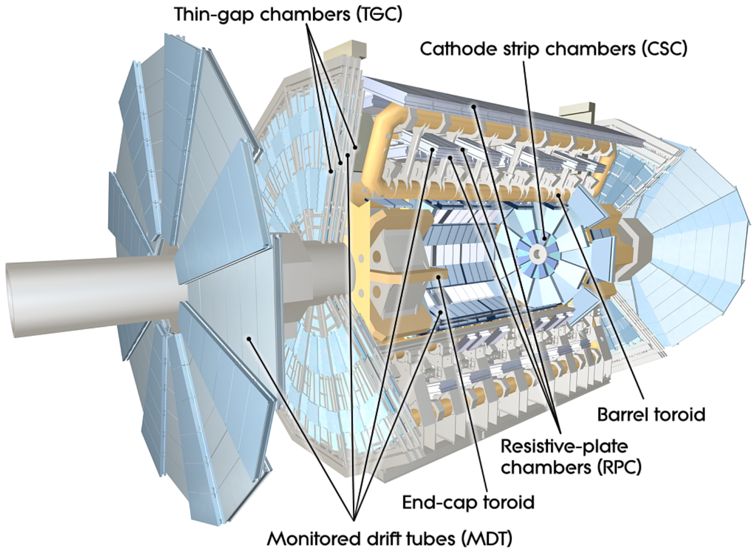

Figure 3.6: Schematic of the ATLAS Muon Spectrometer, taken from [45].

thickness is > 22 radiation lengths[2] in the barrel and > 24 in the end-caps. The resolution in energy is $\Delta E/E = 11.5\%/\sqrt{E} + 0.5\%$ and for ϕ, $\Delta\phi = 50/\sqrt{E}$ mrad, where in both cases the energy is in GeV [48].

Hadronic calorimeter is placed around the EM calorimeter and has 3 parts. The first is the **Tile calorimeter**. It consists of a central barrel ($|\eta| < 1$) and two extended barrels ($0.8 < |\eta| < 1.7$). It uses a steel absorber and scintillator as a sampling material. It has thickness of 9.7 interaction lengths[3].

Further, there is a **LAr hadronic end-cap** placed behind the EM calorimeter end-caps and covers $1.5 < |\eta| < 3.2$ and the whole azimuthal angle ϕ. It uses a liquid argon as the sampling material and copper as the absorber. The jet resolution of the tile and the hadronic end-cap calorimeter is $\Delta E/E = 50\%/\sqrt{E} + 3\%$, where E is in GeV [48].

Finally, the **LAr forward calorimeter** is placed around the beam pipe, covering zenith angles up to $|\eta| = 4.9$. It is 10 interaction lengths long and has three modules: first with a copper absorber for electromagnetic measurement and two made of tungsten for hadrons.

3.5 Muon spectrometer

The Muon Spectrometer measures only muons (strictly speaking high p_{T} muons, which travel far enough to reach it). It consists of 3 barrel layers in 5, 7.5 and 10 meters from the beam pipe and 2×3 end-caps at $\pm 7.9, \pm 14, \pm 21.5$ meters, as can be seen in Figure 3.6. There is also the barrel toroid magnet for $|\eta| < 1.4$, while for $1.6 < |\eta| < 2.7$ there are two smaller end-cap magnets.

There are four subdetectors in the muon spectrometer. The **Monitored Drift Tubes** (MDT) cover the whole η range and measure track coordinates. They are made of aluminium tubes of 30 mm diameter with a cathode wire in the middle, where a position of

[2] Radiation length is a distance during which an electron or a photon loses $1/e$ of its energy.
[3] Interaction length is, similarly to radiation length, a path after which hadron loses a $1/e$ of its energy.

a particle is determined from the drift time of the particle. Further, there is the **Cathode Strip Chamber** (CSC), a multi-wire proportional chamber, which covers the most forward regions $2 < |\eta| < 2.7$ and is more radiation resistive and can operate in a high radiation present near the beam pipe.

The trigger system consists of **Resistive Plate Chambers** (RPC), situated around the barrel, and **Thin Gap Chambers** (TGC), which are located in the end-cap regions. Together they cover $|\eta| < 2.4$. The RPC consists of two strip layers orthogonal to each other, with a gap between them filled with gas. The TGC is a multi-wire proportional chamber with a quick drift time and it is designed to provide a fast estimate of p_{T} of the muon.

3.6 Lepton measurement

Both analyses described in this thesis study leptons in the final state. Therefore, it is important to understand how they are reconstructed and identified by the ATLAS detector.

3.6.1 Muons

Muons are the most penetrating particles and therefore pass trough both calorimeters and leave a track in the muon spectrometer. Thus, there are two tracks per muon, one in the ID and one in the MS. Based on the type of objects used in the reconstruction, there are four types of reconstructed muons in ATLAS. A *standalone* muon is reconstructed only by the MS and can therefore also have $2.5 < |\eta| < 2.7$, outside the ID coverage. The lowest contribution of fake[4] and secondary muons[5] is found in the so called *combined* muons, which are found either by creating two independent tracks in the ID and the MS and then combining them or by extrapolation of track from one detector to the other [58].

Sometimes, e.g. when they have a low p_{T}, muons leave only a segment of a track in the SM. If an ID track can be extrapolated to the segment, then it is identified as a *segment-tagged* muon. Finally, it is possible to identify a muon from ID track and the small amount of muon energy deposited in the calorimeter. Such muon is called *calorimeter-tagged* and has the biggest background [24]. In this analysis, the combined muons are used.

3.6.2 Electrons

Unlike muons, electrons are stopped by the electromagnetic calorimeter, creating an electromagnetic shower. The energy deposited in the calorimeter is divided into cells, which have size 0.025×0.025 in (η, ϕ) space. The cells are then combined to cover the whole shower, creating a cluster. Since such cluster can be also left by a photon, it has to be further matched to a track in the inner detector. Track is considered as matched if the distance of cluster from the tracks in pseudorapidity is $|\Delta\eta| < 0.05$ and distance in azimuthal angle is $|\Delta\phi| < 0.1$.

An energy of the electron is then determined from the energy deposited in the cluster, while the momentum and the direction is determined from the ID information. Electrons have worse reconstruction efficiency than muons (circa 10% lower), because they suffer radiative losses, which also means there has to be a correction for these losses when computing the total energy [59].

[4]Particles misidentified as muons or false signal interpreted as muon.

[5]Secondary muon is a muon not originating from the primary interaction but from e.g. calorimeter shower.

Chapter 4

The photon-induced WW measurement

The second LHC run presents first opportunity for physicist to study collisions at record center-of-mass energies $\sqrt{s} = 13$ TeV. Higher energies lead to higher cross-sections of numerous processes. Together with large luminosity recorded at such energy, new and more accurate measurements become possible.

This thesis summarizes the 13 TeV analysis of the photon-induced exclusive WW production with leptonic decays. In comparison to the previous analysis of this process at 8 TeV, the new measurement has advantage of higher yield.

The first stage of the analysis is the preselection, where the selection is mainly based on detector acceptance. At this point the signal is buried under significant background, which is dominated by Drell-Yan for the ee and $\mu\mu$ channels and by $t\bar{t}$ production for the $e\mu$ channel.

Drell-Yan is, in a leading order, a production of virtual photon or Z boson from annihilation of quarks, where the dilepton final state is the only one relevant to the analysis ($q\bar{q} \to Z/\gamma^* \to l^+l^-$ shown in Figure 4.1b). The $t\bar{t}$ production has many channels where the most important are displayed in Figure 4.2.

The signal is isolated by an exclusivity veto, which requires no additional particles aside from the leptons near the dilepton vertex. At this point, the ee and $\mu\mu$ channels are dominated by the Drell-Yan, while the $e\mu$ channel contains mostly the exclusive diboson events. For this reason, only $e\mu$ final state is considered in the analysis. The other two channels are still useful for derivation of corrections.

Remaining background in the $e\mu$ channel is the Drell-Yan process with $\tau\tau \to e\mu$ final state and inclusive WW production, which is dominated by $q\bar{q} \to W^+W^-$ process (see Figure 4.1a). Since particle multiplicity of both Drell-Yan and inclusive WW is poorly modelled, a correction is derived. Modelling of the Monte Carlo processes is further checked in a control region, which is defined in events with only few particles in proximity of the dilepton vertex.

After application of all the corrections, systematic uncertainties are determined. Finally, total cross-section in the fiducial region is derived.

In this chapter, focus is put on the selection and general corrections. Most of the analysis-specific steps are explained in the following chapters.

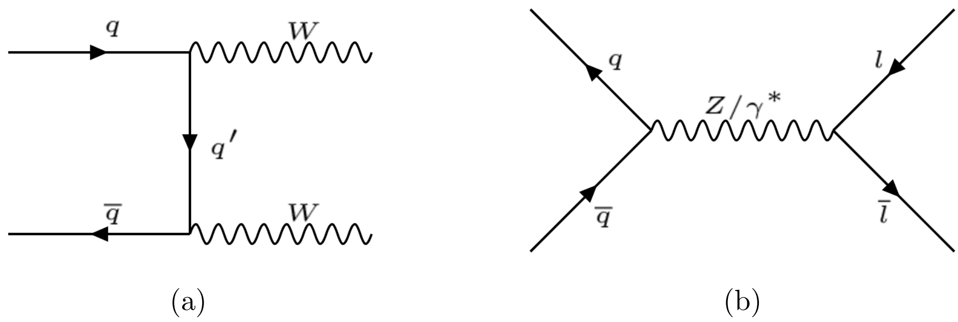

Figure 4.1: Tree level Feynman diagrams of a) dominant channels of inclusive WW production and b) Drell-Yan with two leptons in final state.

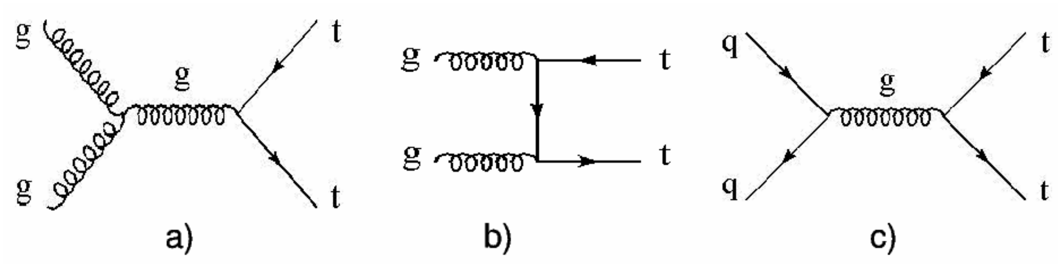

Figure 4.2: Leading Feynman diagrams of $t\bar{t}$ production. Taken from [50].

4.1 Data and Monte Carlo samples

4.1.1 Data

Data used in the analysis are from 2016 data taking of the LHC. Specifically, they are proton-proton collisions with a center-of-mass energy of 13 TeV. Since the detector does not perform perfectly the whole time, some events are of bad quality. List of such events, produced by central data quality group, is kept in Good Run List, which is then used by analyses to exclude corrupted or incomplete events. The total integrated luminosity of events good for physics analysis during 2016 is 33.3 fb^{-1}.

4.1.2 Monte Carlo

Monte Carlos are vital tools in high energy physics, enabling to compare predictions with measurements, used for optimization of selection or estimation of uncertainties. There are many processes contributing to the analysis, which is reflected by the large number of Monte Carlo generators used.

The most important is the signal sample of the $\gamma\gamma \to W^+W^- \to l^+l^-$ process. It is simulated using Herwig 7 generator [51], which uses the EPA mechanism (see Section 2.1) to simulate photon-induced processes. Aside from the exclusive sample, a dissociative production contributes to this process. However, there is currently no available generator capable of simulating dissociation for the WW final state and data driven techniques have been employed to estimate it, which will be expanded on in later chapters.

The dominant background after the full selection is an inclusive WW production. The inclusive sample has numerous processes contributing to it, typically with a significantly larger yield than the signal, but with additional charged particles in the final state. The most important contribution to the inclusive WW background is $q\bar{q} \to W^+W^-$ process, simulated using PowHeg [52], a parton level NLO generator. It is interfaced to Pythia 8 generator [53] for showering and hadronization. Another significant contributor is the $t\bar{t}$ production, which is also generated with PowHeg+Pythia8.

Important background contribution is from the Drell-Yan process. The ee and $\mu\mu$ Drell-Yan production significantly contribute to control regions, which are constructed to control the MC modelling. The hard process is generated using MadGraph generator [54] interfaced with Pythia 8 [53].

Finally, in order to study e.g. the survival factor, $\gamma\gamma \to l^+l^-$ processes are needed. The exclusive production is generated using Herwig++ generator [55]. The single dissociative contribution uses LPair 4.0 [56], while the double dissociative uses Pythia 8.

Aside from the generation of the processes, the evolution of the collision through the detector has to be simulated in order to be able to compare with raw data. For this purpose, the GEANT 4 [57] simulation toolkit is used.

4.2 Analysis selection

As was already mentioned, preselection is designed for Monte Carlo validation in kinematic region mostly restrained by a detector acceptance. First, analysis objects are defined, followed by the event requirements.

4.2.1 Muon selection

Muons are required to pass the requirements of the Combined Muon, which were explained in the previous chapter. Specifically, there is a requirement on the ID track:

- Number of pixel hits+number of crossed dead pixel sensors > 0
- Number of SCT hits+number of crossed dead SCT sensors > 4
- Number of pixel holes + number of SCT holes < 3.
- A successful TRT extension where expected

Furthermore, selected muon has to have a transverse momentum $p_{\mathrm{T}} > 20$ GeV and $|\eta| < 2.4$, where the kinematic range is selected based on detector acceptance and reconstruction efficiencies. In order to ensure the muon does not originate from a jet background, there is selection on d_0 significance, which is defined as $\frac{|d_0|}{\sigma_{d_0}}$ and it has to be smaller than 3.

Finally, there is an isolation requirement in order to reduce multi-jet background, where sum of transverse momentum of additional particles in proximity of the muon has to be significantly smaller than the muon p_{T}. This is done by a dedicated tool, which enables several modes of isolation [58].

4.2.2 Electron selection

Electron candidates are first selected using method described in Section 3.6.2. There are then several quality categories available, starting with *loose*, which has the highest efficiency but also the highest fake contribution, and finishing with *tight*, which has opposite properties. In this analysis, the *medium* quality requirement is used [59].

On the border between the barrel and end-caps, the electrons are reconstructed poorly and are therefore omitted. There is also a pseudorapidity requirement $|\eta| < 2.47$, reflecting the acceptance of both ID and Electron calorimeter. Furthermore, it has to satisfy isolation requirement and the d_0 significance has to be smaller than 5.

Finally, an isolation selection similar to the muon case is implemented, designed to reduce jet background.

4.2.3 Track selection and exclusivity veto

In order to select isolated lepton pairs, the number of tracks in the proximity of the lepton vertex needs to be determined. For this reason, the track selection needs to be properly defined. First, there is a requirement on $p_{\mathrm{T}} > 400$ MeV, which is the standard ATLAS minimal transverse momentum for which the tracking is done in pp collisions with pile-up. Geometrical acceptance of the Inner Detector is reflected in the selection on pseudorapidity $|\eta| < 2.5$

Similar to muon selection, there is a number of requirements on detector hits:

1. Number of silicon hits $>= 9$ (11) if $|\eta| <= 1.65(|\eta| > 1.65)$
2. Number of IBL hits + B-Layer hits > 0
3. Number of pixel holes $= 0$

where the B-Layer is the first Pixel detector layer beyond the IBL. The track selection is the standard collection of requirements used in ATLAS. Finally, two selected leptons are excluded from the track definition.

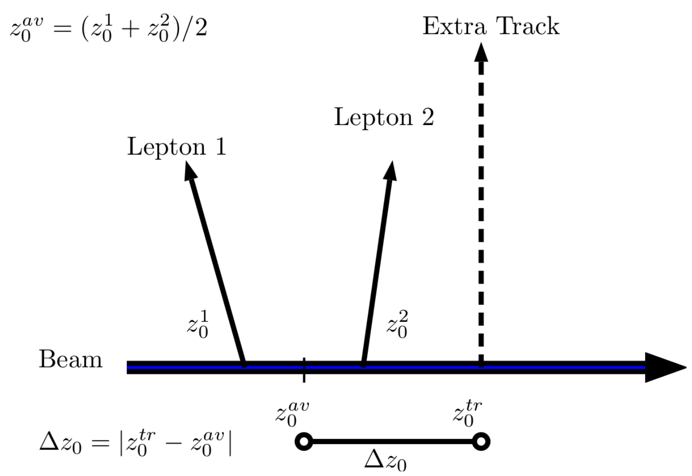

Figure 4.3: Definition of the dilepton vertex and of the window used in exclusive veto selection. Taken from [37].

In contrast to the background processes, the exclusive diboson production contains only two leptons in the final state. Therefore, the first step in isolating the signal from the background is logically to require only two particles in the final state. However, due to the pile-up there is a large number of additional particles produced. Requiring events with only two muons would lead to practically zero yield.

This complication can be bypassed by concentrating only on a region around the dilepton vertex. First, a 1 mm window in the z coordinate is defined around the vertex and number of selected tracks within this window is determined. Then only events with zero additional tracks are required. Such selection stage is also called exclusivity veto and is applied as the last of the event requirements, as will be mentioned in next section.

When counting number of tracks within the window, one can see in Figure 4.4 that apart from the exclusive processes, all other contributors typically produce at least one additional particle. The exclusive veto is therefore a very powerful tool to isolate the exclusive signal.

Note that the particle multiplicity is not well modelled and dedicated corrections need to be derived to properly estimate the background (see Chapter 5).

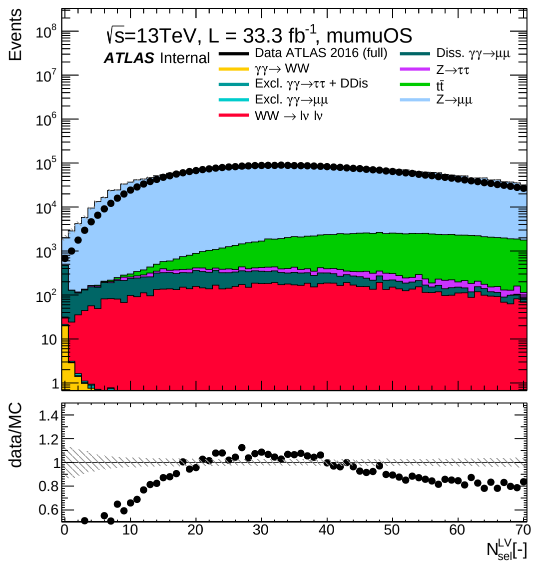

Figure 4.4: Number of additional tracks within $|z_0 \sin\theta| < 1$ mm from the dilepton vertex.

4.2.4 Event selection

In the analysis, lowest unprescaled single lepton triggers are employed. There are two separate triggers for electrons and muons, both with transverse momentum requirement $p_\mathrm{T} > 26$ GeV. To reflect this, every event is required to have two leptons with leading lepton having $p_\mathrm{T} > 27$ GeV, where region between 26 and 27 GeV is ignored due to poor efficiency of the trigger. Also, the dilepton system has to have invariant mass $m_{ll} > 20$ GeV, which excludes poorly modelled regions.

Next, dilepton vertex LV is defined as a point with an average z_0 coordinate of the two leptons (as displayed in Figure 4.3). As can be seen in Figure 4.5, its position is a little different from position of the primary vertex PV for exclusive processes. This is mainly due to pile-up, where the algorithm used to reconstruct vertices wrongly associates pile-up track with the dilepton vertex. This is usually not that important, since most processes have larger number of particles in the primary vertex and position of the vertex is therefore determined with a good precision. However, with only two leptons in the final state, even single additional track wrongly associated with the primary vertex may significantly shift its position.

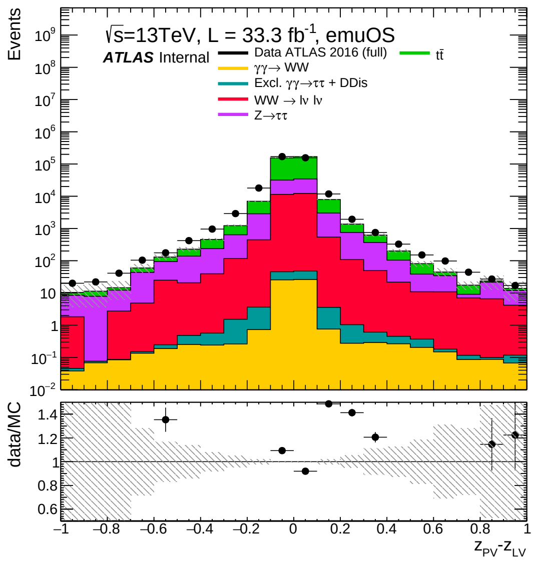

Figure 4.5: Distribution of distance of the dilepton vertex from the primary vertex.

Considering the short lifetime of the W bosons $\tau \approx 3 \cdot 10^{-25}$ s, the final-state leptons are produced at practically one spot. Taking the resolution of the track reconstruction into account, this is reflected by a requirement on the distance of the lepton from the dilepton vertex $|(z_{\mathrm{LV}} - z_{\mathrm{lepton}})| \sin\theta_{\mathrm{lepton}} < 0.5$.

The two selected leptons must also have an opposite charge. In the signal extraction only $e\mu$ channel is considered, but the ee and $\mu\mu$ are still relevant for checks and corrections mentioned later.

Distribution of invariant mass and p_{T} of the lepton pair can be found in Figure 4.6 and additional figures are in Appendix A. The simulation is in satisfactory agreement with data. Notice how insignificant the signal is at this stage, with expected yield in the orders of tens of events. There is also a disagreement for low masses in $e\mu$ channel which needs to be investigated.

The requirements mentioned up to this point will be collectively denoted as a preselection. There is also selection on transverse momentum of the dilepton pair. Requiring $p_{\mathrm{T}}^{ll} > 30$ GeV suppresses significantly contribution of the Drell-Yan.

Finally, the exclusive selection is applied, requiring no selected track in the exclusive window as described in Section 4.2.3. The are 62 events found in data after the veto, which is an improvement compared to 23 events found at the 8 TeV analysis [37].

4.3 General Monte Carlo corrections

Simulation of detector effects is often imperfect and there can be large differences between data and Monte Carlo. Therefore, a vast number of corrections is applied on Monte Carlo to improve the agreement.

Large number of correction prescriptions is centrally produced by dedicated ATLAS groups. The most relevant to this analysis are summarized in this section. Each of the corrections has a systematic uncertainty, which has to be accounted for when determining the final results. Systematic uncertainties will be discussed in more detail in another

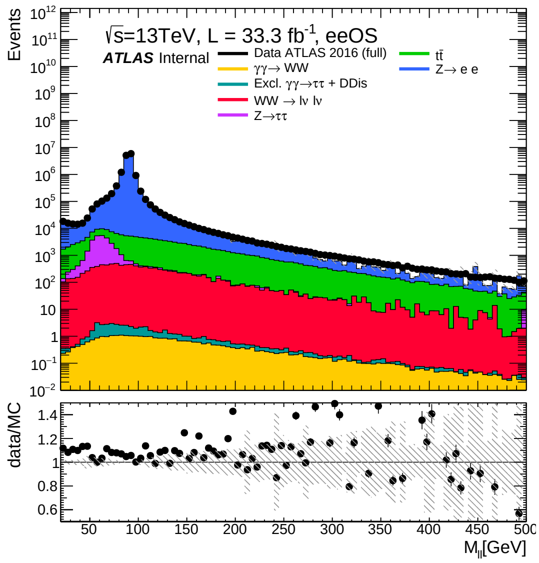

(1a)

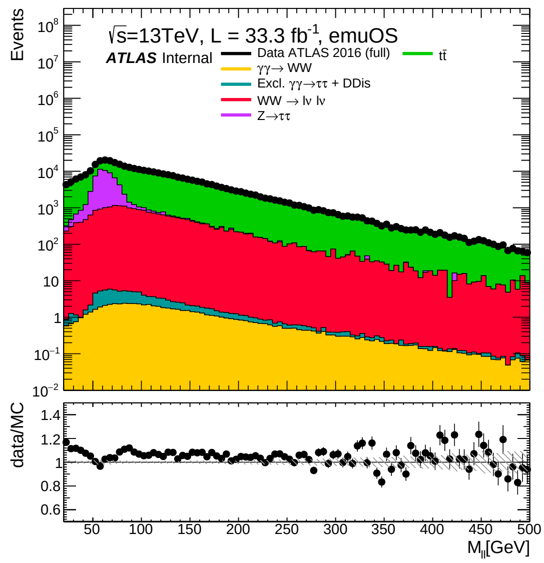

(1b)

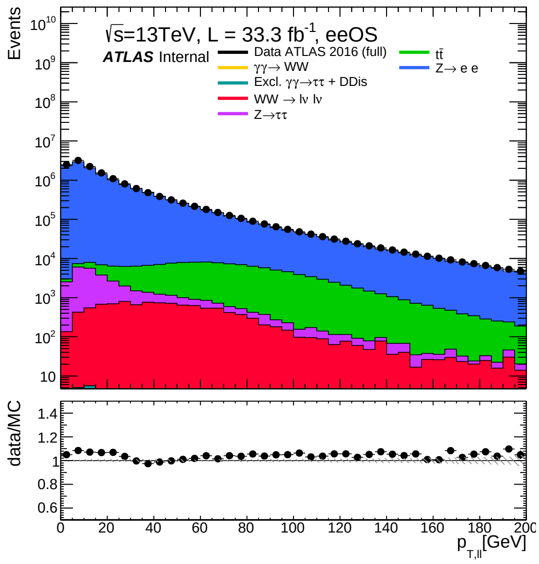

(2a)

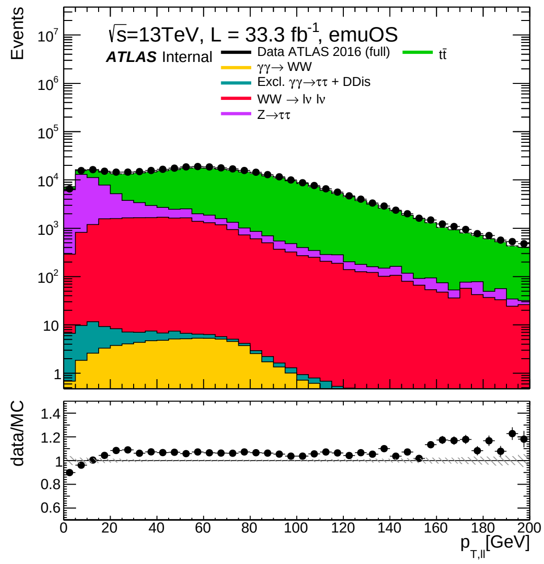

(2b)

Figure 4.6: Distributions of data and Monte Carlo as a function of 1) invariant mass and 2) p_{T} of the lepton pair for a) ee and b) $e\mu$ channel after the preselection.

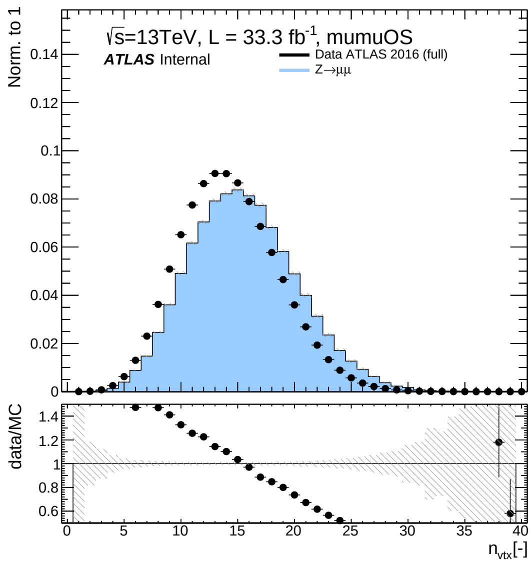

Figure 4.7: Distribution of number of vertices in dimuon channel, comparing data to Monte Carlo. The reweighting of MC was applied with μ scaled by 1/1.09.

chapter. Furthermore, analysis specific corrections were derived, which will be summarized in Chapter 5.

Pile-up: The production of Monte Carlo is launched before data-taking and since exact pile-up is not known in advance, there can be a significant difference between data and MC. Therefore, a dedicated correction is applied by means of event weight made to match vertex multiplicity in data and Monte Carlo. Ideally, each event is weighted based on number of interactions per bunch crossing, μ, in the Monte Carlo to match its distribution in random data-taking period in data.

However, this leads to some disagreement in number of vertices $n_{\rm vtx}$ after these corrections, which is a variable we are more interested in. Therefore, the μ value in data, used when determining the weight, is scaled by 1/1.09 to achieve better agreement. The scale factor reflects the imperfection in the modelling of the visible fraction of the inelastic cross-section.

This correction is not perfect, difference between simulation and data being on the 1σ side of the systematic uncertainty of the correction. Distribution of events after the correction as a function of $n_{\rm vtx}$ can be found in Figure 4.7.

It was found that with factor 1/1.2 the agreement would be better; however it was recommended to us to leave the default value since it will be soon updated by a dedicated group to better describe the data.

Trigger efficiency: Difference between trigger efficiencies is corrected an event weight applied to MC. For example, in case of muon triggers, the ratio of data and MC efficiency (scale factor) is determined for each selected muon. Scale factors for each relevant objects are then combined and used as a weight for each event.

Track impact parameter resolution: There is a slight difference between data and Monte Carlo in resolution of the d_0 and z_0 coordinate. Using this difference the Monte Carlo is smeared using a random generator to better match data.

4.3.1 Muon related corrections

Efficiencies and scale factors of muons (and electrons) are derived using Tag and Probe method in Z and J/ψ resonances [58, 59].
Muon momentum scale and resolution: p_{T} of a muon is corrected for differences in momentum scaling and smeared based on a difference in the muon resolution between data and Monte Carlo.
Muon selection efficiency: There are two stages of the muon selection - requirement on the quality of muon and on the muon isolation. Each stage has its efficiency and has to be corrected for a difference between data and Monte Carlo. This is done using event weight for each muon and each selection:

$$w = \prod_{i=1}^{n_{\mathrm{muons}}} w_i^{\mathrm{quality}} \cdot w_i^{\mathrm{isolation}}$$

4.3.2 Electron related corrections

Electron energy scale and resolution: Since electromagnetic calorimeter does not record the deposited energy perfectly, there has to be a scaling of the recorded energy to more accurately describe the energy of the particle. The difference in the scaling between data and MC is done by correction of the energy in Monte Carlo.
Electron selection efficiency: In case of electrons, the correction is divided into three stages - electron reconstruction, identification and isolation. Each stage has its scale factor, which is then used as an event weight calculated as a product of the different contributions.

Chapter 5

Analysis-specific corrections

This chapter provides an overview of improvements to the modelling of signal and background Monte Carlo. First, modelling of the exclusivity veto is studied. Then, the disagreement of particle multiplicity between data and Drell-Yan Monte Carlo is improved using reweighting. This approach is validated in a control region, where the background is compared to data and remaining difference is fixed. In the last part, the signal Monte Carlo is adjusted to include the effect of the survival factor and to estimate the fraction of the dissociative production.

5.1 Exclusive efficiency

In order to correctly assess the cross-section, one needs to estimate the efficiency of the exclusive selection. One could of course use the signal Monte Carlo and simply calculate the fraction of events which pass the veto, but this method assumes that the MC perfectly describes data. As we will see, this is not the case and data driven method needs to be used.

Previous exclusive dilepton and diboson analyses [29, 37] employed a simplistic method. For each event, a random point[1] well separated from the primary vertex is found (using cut on longitudinal distance) and the exclusivity veto is checked there. This estimated the probability of a pile-up track appearing within the 2 mm windows of the exclusive selection. The efficiency was studied as a function of number of vertices n_{vtx} to illustrate dependence on the pile-up.

However, there is a problem with this method. Veto on the distance from the primary vertex biases the position of the random point towards larger z values, where the particle activity is smaller than at the primary vertex. To account for this, we parametrized the efficiency also as a function of the z. For each event, only z windows which are sufficiently far from the LP are used. The distribution is normalized as a function of z and now describes the dependence of the exclusive efficiency on z: $\epsilon_{\mathrm{excl}}(z, n_{\mathrm{vtx}})$. The dependence of the exclusive efficiency on n_{vtx} is obtained by an integration over the z is performed, weighted by a probability of finding a vertex at coordinate z ($P_{\mathrm{vtx}}(z)$):

$$\epsilon_{\mathrm{excl}}(n_{\mathrm{vtx}}) = \int \epsilon_{\mathrm{excl}}(z, n_{\mathrm{vtx}}) P_{\mathrm{vtx}}(z) \mathrm{d}z$$

This method was validated against the efficiency derived in the dilepton vertex of the exclusive Monte Carlo.

[1] Position of the random point was based on the distribution of the vertices along the beam pipe. Such distribution has approximately Gaussian shape.

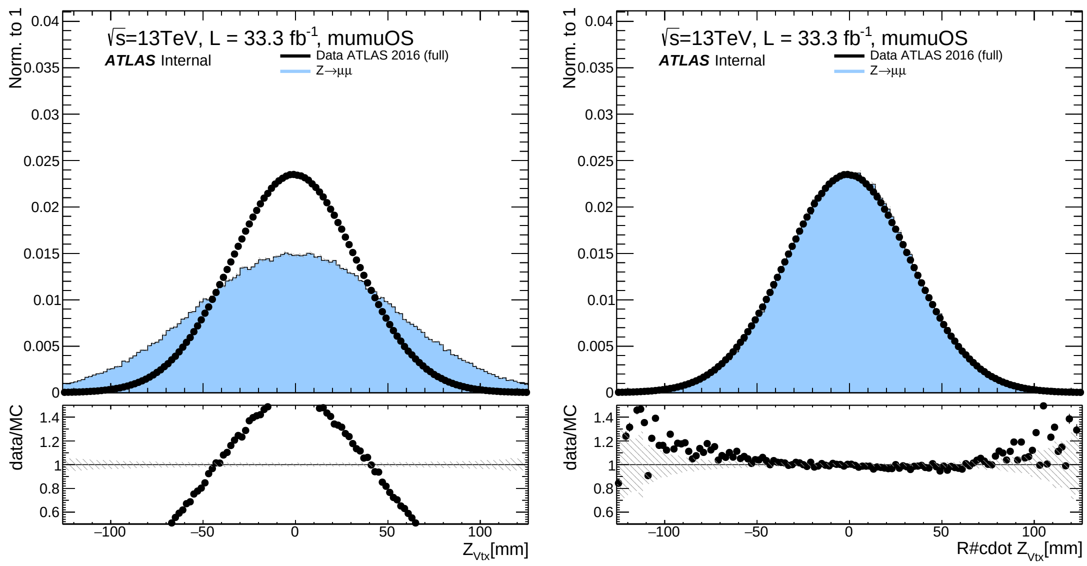

(a) (b)

Figure 5.1: Distribution of vertices as function of the z coordinate (a) before and (b) after beam spot scaling correction was applied.

When comparing Monte Carlo to data, there is a 12% difference in the efficiencies. It was found out that this discrepancy is to a large extent connected to distribution of the vertices as function of the z coordinate (also called beam spot distribution), which is significantly different in data and Monte Carlo.

5.1.1 Vertex distribution disagreement

The beam spot distribution can be found in Figure 5.1a and at first glance there is a significant disagreement between data and MC. The most precise way to correct it would be to produce a new Monte Carlo with an updated beam spot information, but simulation of all the samples would take too long to be completed to be relevant for this thesis.

The solution we use (at least until new Monte Carlo with better z distribution is provided) is based on scaling of the event z coordinates. Using a Gaussian fit the beam spot distribution in both data and MC is fitted. The variance of the beam spot is found to be $\sigma_{\mathrm{BS}}^{\mathrm{data}} = 34.021 \pm 0.006$ mm for data and $\sigma_{\mathrm{BS}}^{\mathrm{MC}} = 52.73 \pm 0.06$ mm for the Monte Carlo. Their ratio is then taken as the scaling factor, which is applied on z coordinate of both tracks and vertices in Monte Carlo.

The resulting effect can be seen in Figure 5.1b. Though not ideal, the correction leads to a significant improvement in the agreement of data and Monte Carlo. This method is however not perfect, since it changes the resolution in z of the objects. Also, there is still a disagreement between data and Monte Carlo.

5.1.2 Updated efficiency

After application of the z scaling, the exclusive efficiency is studied as a function of number of vertices n_{vtx}. Figure 5.2 shows efficiency derived for data, signal MC and Drell-Yan MC together with efficiency derived in dilepton vertex of the signal exclusive MC. The agreement between the two methods for the exclusive Monte Carlo validates the method, while the agreement with Drell-Yan proves the method is valid also for processes with large particle multiplicities and does not bias the efficiency.

The disagreement with data is 5% when averaged over the n_{vtx} distribution, which is currently taken as a systematic uncertainty on the Monte Carlo modelling. However, there is an effort to improve the agreement, for example by studying how the beam spot varies within different periods of data-taking.

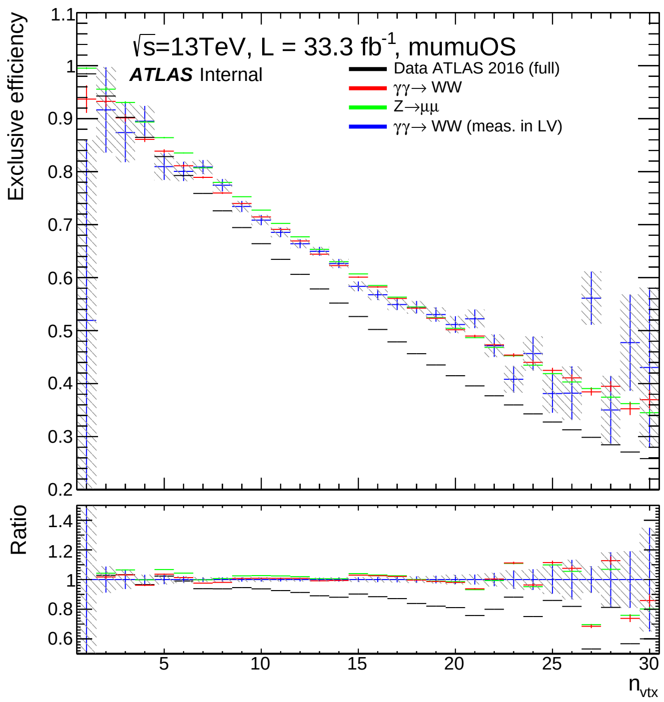

Figure 5.2: Exclusive efficiency, comparison between data and two Monte Carlo samples and directly derived efficiency of the signal MC.

5.2 Drell-Yan multiplicity correction

As was demonstrated in the previous chapter (see Figure 4.4), the particle multiplicity of Drell-Yan in proximity of the dilepton vertex is not well simulated. A data driven correction is therefore used to determine a weight $w(n_{\text{ch}})$ which is then applied in the Monte Carlo.

The weight is a ratio of charged particle multiplicity in data $f^{\text{data}}(n_{\text{ch}})$ and Monte Carlo: $f^{\text{MC}}(n_{\text{ch}})$:

$$w(n_{\text{ch}}) = \frac{f^{\text{data}}(n_{\text{ch}})}{f^{\text{MC}}(n_{\text{ch}})}$$

Since particle distribution in data is not known, it has to be measured. First, contribution of the pile-up to the track multiplicity is subtracted. Then, the spectrum is converted to particle level using Bayesian unfolding. The method used in this analysis is inspired by the one used in study of underlying event in inclusive Z production [60].

The multiplicity is studied for Drell-Yan with two muons in final state. The selection is identical to preselection and the $p_{\text{T}}^{ll} > 30$ GeV requirement since particle multiplicity varies with p_{T}^{ll}. Furthermore, only events in proximity of the Z mass peak are chosen (70 GeV $< m_{ll} <$ 105 GeV).

5.2.1 Correction for pile-up

To correct the track multiplicity for contribution of pile-up, one has to determine distribution of tracks from additional pp interactions. Similarly to exclusive efficiency it depends on the z coordinate. For higher values of z it is less likely one will find a pile-up vertex and therefore the activity is lower.

To avoid any biases from the hard event, multiplicity is first determined as a function of z where region around the primary vertex is ignored. This distribution is then convoluted with distribution of vertices in z. Resulting distribution determines probability of finding n pile-up tracks in 2mm ΔZ windows, which we will designate as $P_{PU}(n)$.

Probability of finding n measured tracks $P_{all}(n)$ in an event can be interpreted as:

$$P_{all}(n) = \sum_k P_{hard}(k) \cdot P_{PU}(n-k),$$

where $P_{hard}(k)$ is a probability of finding k (primary) tracks from the studied hard process (in our case Drell-Yan), which is the distribution we would like to determine. Interpreting the pile-up contribution $P_{PU}(n-k)$ as a matrix $U_{n,k}$, one can invert the relation in the following way:

$$P_{hard}(n) = \sum_k U^{-1}_{n,k} P_{all}(k),$$

where all distributions on the right side are now known.

This method was validated in Monte Carlo by comparing the corrected distribution to that of tracks matched to the particles of the hard event. Reconstructed distribution and distribution corrected for the pile-up are compared to multiplicity of tracks matched to particles of hard event in Figure 5.3. There is a good agreement and the method can be used to subtract pile-ip from data track multiplicity.

Next, the distribution of primary tracks has to be corrected to particle level. For this purpose, an unfolding procedure is applied.

5.2.2 Unfolding

Unfolding is a procedure used to unsmear (unfold) detector effects from the reconstructed spectrum to produce a spectrum at particle level.

The basic idea of unfolding assumes some correspondence matrix M between the truth T and reconstructed spectra R such that $R = MT$ (assuming no background). Such matrix would simulate e.g. effects of a detector. To get the opposite relation, one could start with a simple inversion of the matrix M and using relation $T = M^{-1}R$. This method is not ideal, it for example tends to amplify small statistical fluctuation as a presence of a signal [61].

Usual method used for unfolding at the LHC is called Bayesian unfolding. Let us rewrite the matrix correspondence in language used in statistics, assuming discrete distributions:

$$P(T_i) = \sum_j P(T_i|R_j)P(R_j),$$

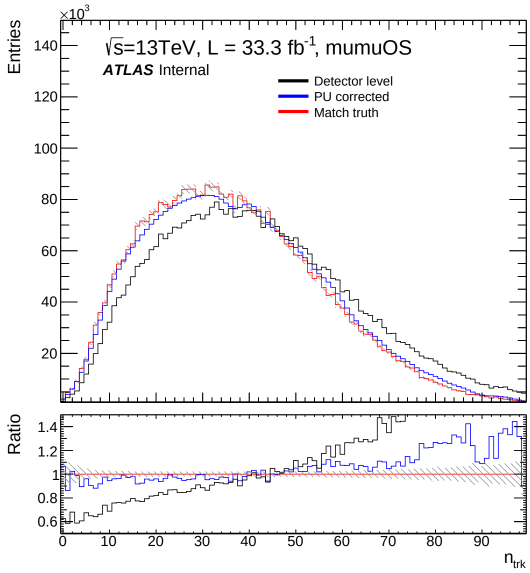

Figure 5.3: Distribution of number of tracks before and after pile-up subtraction compared to distribution of tracks to primary particles.

where $P(T_i)$ is distribution of truth, $P(R_j)$ distribution of reconstructed spectra and $P(T_i|R_j)$ is probability of T_i given R_j. This can be rewritten using the Bayes formula as:

$$P_1(T_i) = \sum_j \frac{P(R_j|T_i)P_0(T_i)}{\sum_k P(R_j|T_k)P_0(T_k)} P(R_j).$$

Now the $P_0(T_i)$ is our prior assumption of the truth distribution, while $P_1(T_i)$ is our new estimate. Hence, by iterating this method one gets better estimation of the truth spectra:

$$P_{r+1}(T_i) = \sum_j \frac{P(R_j|T_i)P_r(T_i)}{\sum_k P(R_j|T_k)P_r(T_k)} P(R_j).$$

5.2.3 Correction to particle level

With unfolding at our disposal, it is simply a matter of its application to obtain the truth spectra. Ratio between the unfolded data and Monte Carlo particle spectra is displayed in Figure 5.4. Their ratio will be used as a weight in the Drell-Yan Monte Carlo. The correction is large for low values of n_{ch}.

The track multiplicity in vicinity of the primary vertex after the correction can be found in Figure 5.5. The generated spectra are now in much better agreement. Remaining differences are studied in the next section.

5.3 Background estimation

After the exclusivity veto, the only significant backgrounds are Drell-Yan with $\tau\tau$ in the final state and inclusive WW. To verify that they are indeed modelled correctly, a data driven-estimate is used. First, one has to define a control region. It has to be kinematically close, but still orthogonal to our final selection. To achieve this, we used the same selection

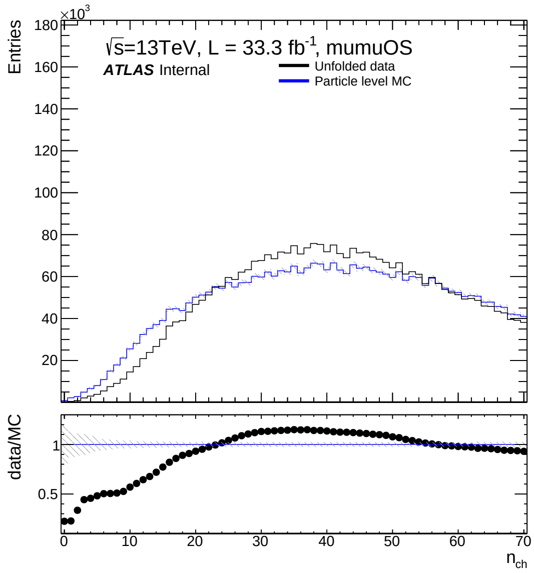

Figure 5.4: Unfolded track multiplicity for data and particle multiplicity for Monte Carlo. Their ratio is taken as an event weight to correct the Monte Carlo.

as for the signal up to the exclusivity veto. Then, instead of no track in the 2 mm window, 1-4 tracks are required.

An assumption is made in the background estimation that differential distribution is modelled with satisfactory precision, and only normalization is studied. This is done using template likelihood fit of Monte Carlo to data.

5.3.1 Likelihood fit

When some parameter α of a probability distribution of a random variable $f(x, \alpha)$ is unknown (for example normalization in our case), it can be studied using a likelihood:

$$L(\alpha) = f(x = x_{data}, \alpha).$$

The estimator of the parameter α is such a value of the parameter for which the likelihood is maximal. For convenience, a minus logarithm of the likelihood is often used and the minimum is required instead. We then search for $\hat{\alpha}$ satisfying $\frac{\mathrm{d}L}{\mathrm{d}\alpha}|_{\alpha=\hat{\alpha}} = 0$. The variance of the parameter can be estimated using Rao-Cramer-Frechet inequality leading to:

$$\hat{\sigma}_{\hat{\alpha}} \geq \left(\frac{\mathrm{d}^2 \ln L}{\mathrm{d}\alpha^2} \right) \Bigg|_{\hat{\alpha}},$$

where the equality holds for a large statistics. It can be interpreted as a value of $\hat{\sigma}_{\hat{\alpha}}$ for which $\ln L(\hat{\alpha} \pm \hat{\sigma}_{\hat{\alpha}}) = \ln L(\hat{\alpha}) - \frac{1}{2}$ when considering the Gauss distribution.

The maximum likelihood method has an advantage that it is unbiased for a large number of data points N (meaning $\alpha \to \alpha_0$ for a large number of events, where α_0 is the true value of the parameter) and efficient ($\left\langle (\alpha - \alpha_0)^2 \right\rangle$ is small for large N) [63].

5.3.2 MINUIT

MINUIT [66] is a common tool for likelihood or χ^2 fits used in High Energy Physics. Since most likelihood problems cannot be computed analytically, such tool is necessary to

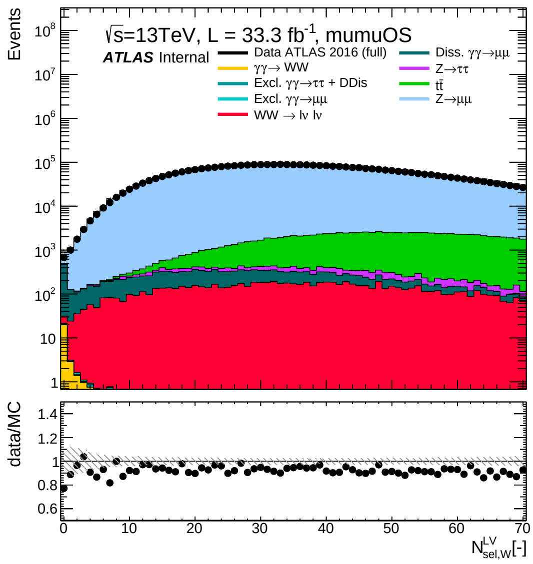

Figure 5.5: Number of additional tracks within $|z_0 \sin\theta| < 1$ mm from the dilepton vertex for events passing the preselection and $p_{\mathrm{T}}^{ll} > 30$ GeV requirement.

perform numerical computations of the likelihood minimization. Since more local minima can exist, it is useful and almost necessary to estimate the initial values of the parameters. This could in our case be result from previous analyses or a theoretical prediction.

The MINUIT uses function **MIGRAD** to find the minimum. There are then two ways to estimate the uncertainties. First is **HESSE**, which produces symmetric errors through parabolic extrapolation at minimum and is based on the Rao-Cramer-Frechet inequality. The second method is **MINOS**, which searches for points where $\ln L(p \pm \sigma) = \ln L_{min} + \frac{1}{2}$. The second method is slower but more precise and can produced asymmetric error. Example of situation where this can lead to significant difference is in Figure 5.6. The tool also computes correlation coefficient and allows for multidimensional fits.

5.3.3 Drell-Yan $Z \to \tau\tau$ and inclusive W^+W^- estimation

Distribution of events as a function of p_{T}^{ll} before and after the likelihood fit can be found in Figure 5.7. The fit was done for the Drell-Yan and inclusive WW and the uncertainties were derived using the **MINOS** method.

The derived scaling factors are found to be:

- **Drell-Yan $Z \to \tau\tau$:** $S_{\mathrm{fit}}^{Z\to\tau\tau} = 0.861 \pm 0.035$
- **Inclusive W^+W^-:** $S_{\mathrm{fit}}^{\mathrm{Incl.}W^+W^-} = 1.007 \pm 0.062$

These factors are applied in the Monte Carlo after the signal selection and the uncertainty contributes to the systematic uncertainty of background modelling.

5.4 Size of dissociative contribution

As was mentioned earlier, there is no Monte Carlo available capable of generating the dissociative component of the exclusive WW production. To compensate for its absence,

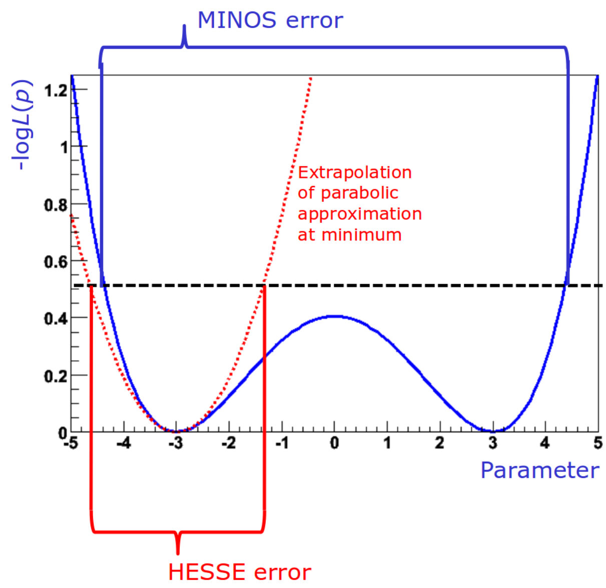

Figure 5.6: Comparison of error estimation through HESSE and MINOS errors. Taken from [64].

the exclusive Monte Carlo is scaled by a factor measured in data. The factor represents fraction of events contributing in the dissociative channels. Additionally, beforehand mentioned survival factor, which takes into account possible strong interaction taking place aside the photon one, needs to be assessed.

These factors can be determined together using the photon-induced dilepton production, the only other exclusive diphoton process with a sufficient yield. Also, its dissociative component is available, which is useful in case of validation studies.

A region with similar kinematic properties to the signal selection must be used. One cannot simply study the exact same final state for following reasons:

1. Neutrinos from WW decay carry away part of the energy and momentum. Therefore, the invariant mass of the dilepton pair in WW is not equivalent to the invariant mass of the photons. This is only the case for the exclusive dilepton production.

2. The W has much larger mass then any of the relevant leptons. Hence, in order to produce two W bosons, the invariant mass of the $\gamma\gamma$ system has to be equivalent to two masses of W: $m_{\gamma\gamma} > 2 \times m_W \approx 160$ GeV. For the production of dileptons the invariant mass of $\gamma\gamma$ is the same as the mass of the dilepton pair $m_{ll} = m_{\gamma\gamma}$.

From those conditions it is clear that one cannot use the same selection as in the diboson analysis to described the same phase-space. But one can get sufficiently good approximation with the following requirements:

- Selection for leptons as is used in the diboson analysis
- ΔZ requirement and exclusivity veto to isolate the dilepton process
- The invariant mass of the dilepton system $m_{ll} > 160$ GeV

This selection is very similar to the one used in the dilepton analysis (see Chapter 7) except for the absence of the $p_{\mathrm{T}}^{ll} < 1.5$ requirement.

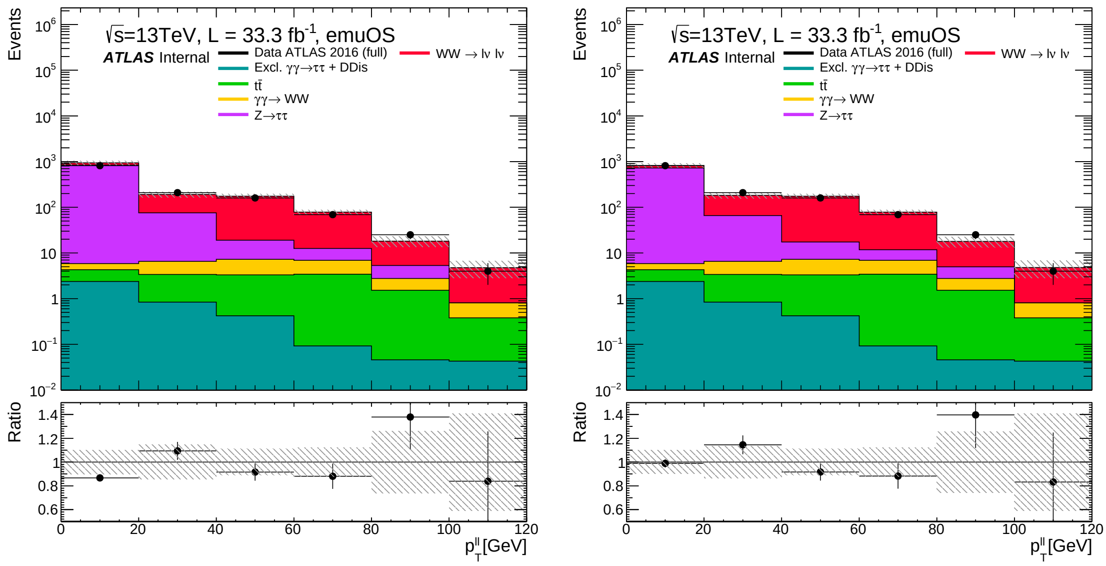

Figure 5.7: Distribution of events as a function of the transverse momentum of the dilepton system after preselection and the requirement on 1-4 additional tracks in the proximity of the dilepton vertex. On the left is distribution before the fit in the control region, on the right after.

After this selection, one simply measures the yield in data N_{data} and subtracts background (Drell-Yan) N_{DY}, which is determined from Monte Carlo. The scale factor is then simply:

$$S_{\text{excl}} = \frac{N_{\text{data}} - N_{\text{DY}}}{N_{\text{excl}}},$$

where N_{excl} is contribution of the signal Monte Carlo (excl. $\gamma\gamma \to ll$). This value was derived using the $\mu\mu$ channel and is found to be $S_{\text{excl}} = 3.39 \pm 0.23$.

The scale factor is studied as a function of several variables. For example, an invariant mass dependence was derived. Within the statistical uncertainties no change with the mass is observed above $m_{ll} > 160$ GeV, as can be seen in Figure 5.8.

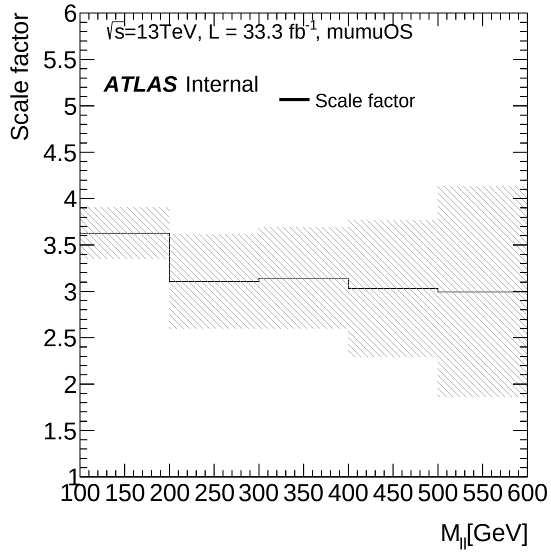

Figure 5.8: Exclusive sample scale factor as a function of the invariant mass m_{ll}.

Chapter 6

Results and systematic uncertainties

Every correction and selection, described in previous chapters, comes with some uncertainty, which needs to be considered in the discussion of the results. They are divided in two parts: uncertainties of ATLAS tools and analysis-specific uncertainties.

In Section 6.2, the differential distributions are shown to demonstrate the level of modelling of data. The chapter ends with derivation of the cross-section and discussion of the results.

6.1 Systematic uncertainties

Systematic uncertainties are with few exceptions treated in the following way: Some aspect of analysis, e.g. some weight, is varied to emulate change by $\pm 1\sigma$. Difference in comparison to the original (nominal) distribution is then taken as a systematic uncertainty. Since most systematics are varied in two directions, there are up and down variations, leading to asymmetric uncertainties. Individual uncertainties are then summed in quadrature to get total uncertainty.

6.1.1 Pile-up reweighting uncertainty

The biggest contribution from the systematic uncertainties provided by the ATLAS group is from the pile-up reweighting. As was already noted in Section 4.3, the nominal value of the correction has poor agreement with data. The uncertainty is assessed from variation of the data scale factor.

6.1.2 Luminosity uncertainty

The luminosity uncertainty originates from the precision of the van der Meer scan and its recommended value is 3.4% [68].

6.1.3 Muon related uncertainties

Efficiency Scale Factors: Each scale factor used to correct the muons has some statistical and systematic uncertainty. The effect on the results is obtained by varying the scale factor by 1σ for all the uncertainties. This concerns scale factors from trigger efficiency, reconstruction efficiency and isolation efficiency.

Momentum scaling: The factor used to scale the momentum is varied within its uncertainty.
Momentum resolution: The smear factor used on the muon is smeared by 1σ. This is done independently for track from Inner Detector and from the Muon Spectrometer.

6.1.4 Electron related uncertainties

Efficiency Scale Factors: Similarly to the case of muons, each electron scale factor - reconstruction, identification, isolation and trigger - is varied based on its uncertainty. However, contrary to muon case, electron efficiencies are divided into several p_{T} and η regions, also differentiating between correlated and uncorrelated systematics.
Energy scaling and resolution: Once again the energy scaling factor and resolution is varied based on its uncertainty. The uncertainties are studied in several p_{T} and η regions.

6.1.5 Track related uncertainties

Track Reconstruction Efficiency: The biggest uncertainty of the track reconstruction comes from the limited knowledge we have about the material in the detector. Hence, in order to assess the uncertainty in the modelling of tracks, material of the Inner Detector is scaled and difference in the efficiency is determined. The obtained uncertainty is propagated to the analysis by randomly removing tracks based on the difference. The variation of results compared to the nominal distributions determines the systematic uncertainty.
Fake rate: The uncertainty of the contribution of fake tracks can be quite large (124% in our case) and its only thanks to their rare occurrence that they do not significantly contribute to the overall uncertainty. The effect is once again determined by randomly removing tracks based on the difference between nominal and scaled efficiency.

6.1.6 Uncertainties of analysis-specific methods

Here, the analysis specific uncertainties are summarized:
Exclusive efficiency: Since the statistical uncertainty is negligible, the considered uncertainty includes only the bias of the method used to derive the efficiency. It is derived in Monte Carlo and found to be 1.6%.
Background modelling: The uncertainty of the fit is taken as a systematic uncertainty of the Drell-Yan and inclusive WW scale factor.

6.2 Final distributions

The signal is studied after the final selection described in Section 4.2. Number of events after each selection stage (preselection, $p_{\mathrm{T}}^{ll} > 30$ GeV and exclusivity veto) can be found in Table 6.1. In the signal region, the Monte Carlo predicts 63.7 events and we observe 62 events in data.

The main distributions in the signal region can be found in Figure 6.1 and 6.2. They show a good agreement between data and Monte Carlo within the statistical uncertainties of the measurement, not only in the total yield but also in the differential dependence. The dominant background is inclusive WW production with small contribution from Drell-Yan process.

A slight disagreement can be seen in 6.2b for $0 < \eta < 0.5$, but the difference is still within 2σ of statistical uncertainty and therefore not in any way significant.

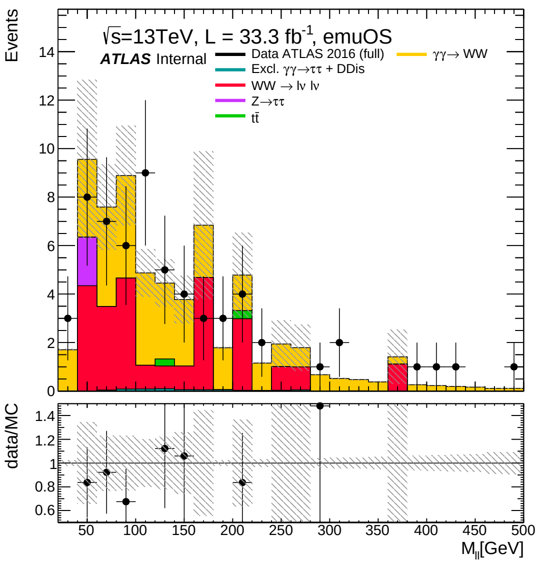

(1a)

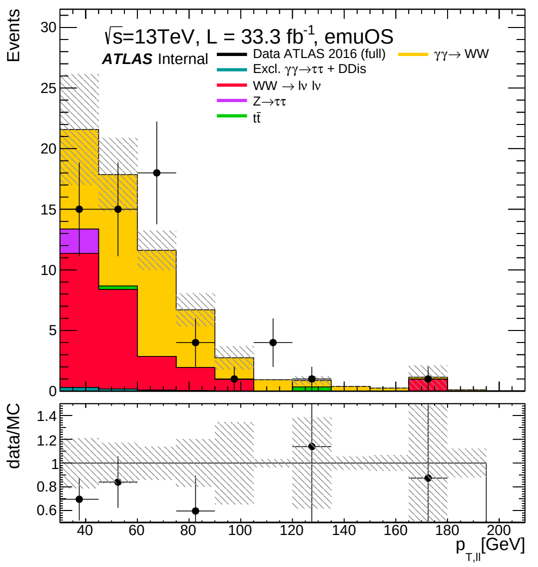

(1b)

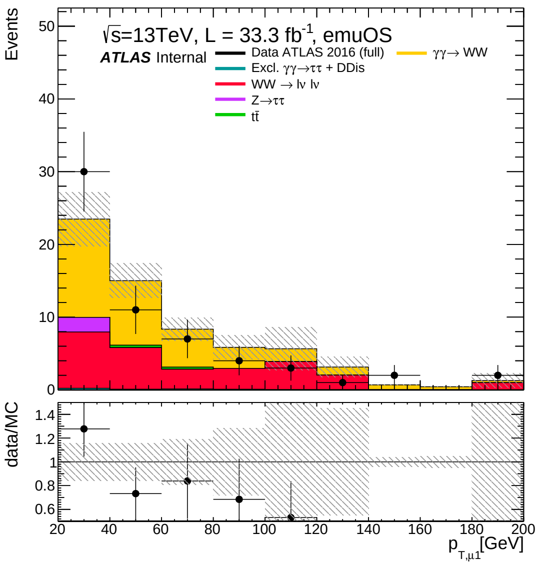

(2a)

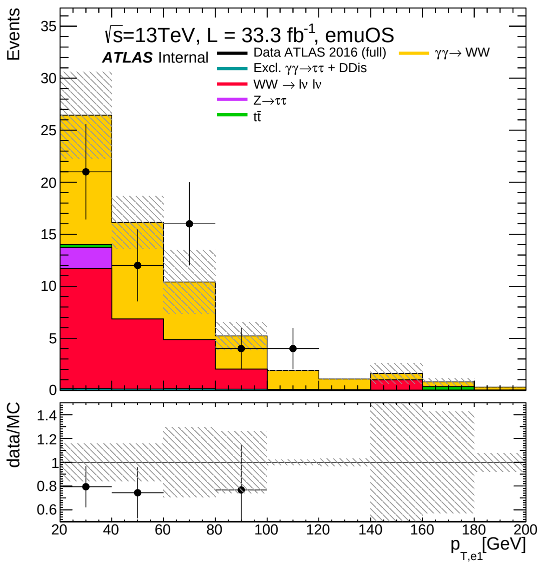

(2b)

Figure 6.1: Final distributions after the full signal selection as a function of (1a) invariant mass, (1b) transverse momentum of the dilepton system, (2a) muon transverse momentum and (2b) muon pseudorapidity. The grey shading represents statistical uncertainty of Monte Carlo, while the black vertical lines are statistical uncertainties in data.

	Preselection	$p_{\mathrm{T}}^{ll} > 30$ GeV	Exclusivity veto
Drell-Yan	50060	9830	2 ± 2
$t\bar{t}$	269980	23625	0.63 ± 0.45
Inclusive WW	25020	17970	25.6 ± 5.7
Exclusive WW	76.45	60.21	35.46 ± 0.19
MC total	345140	264110	63.7 ± 6.0
Data	364329	281574	62

Table 6.1: Number of events for all relevant Monte Carlos and data after each selection stage. The values are rounded to two significant digits of the corresponding statistical uncertainty.

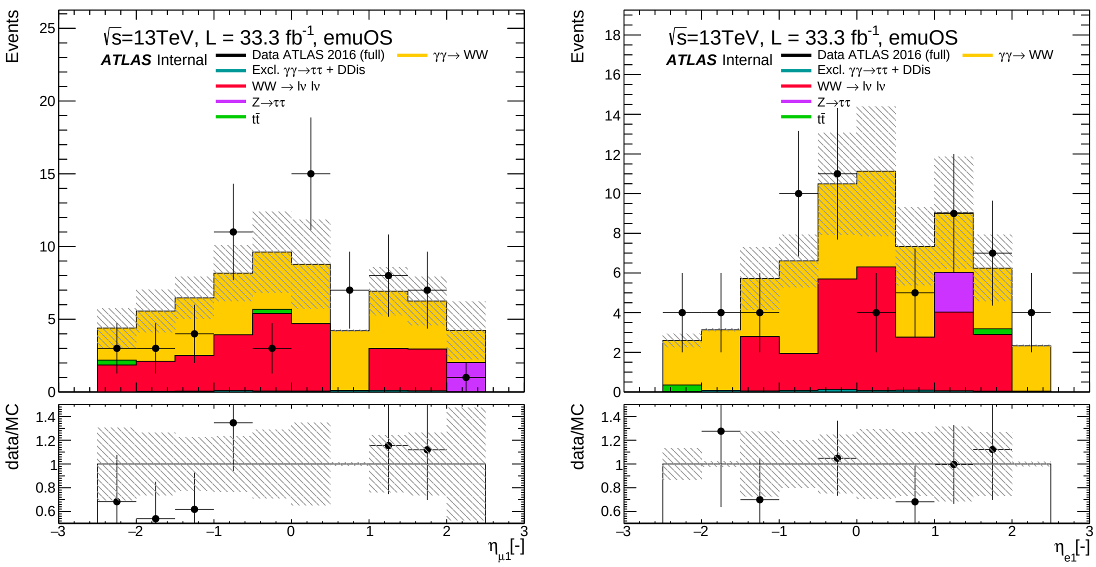

(a) (b)

Figure 6.2: Final distribution after the exclusive selection as a function of (1a) electron transverse momentum and (1b) electron pseudorapidity. The grey shading represents statistical uncertainty of Monte Carlo, while the black vertical lines are statistical uncertainties in data.

6.3 Cross-section extraction

In order to determine the cross-section, one must use Monte Carlo to determine the size of detector effects on measured observable and correct the measured data. To minimize the reliance on the MC, the cross-section is measured in a fiducial region which is kinematically close to the final selection.

6.3.1 Definition of fiducial region

Definition of the fiducial region reflects restrictions imposed by the triggers and detector acceptance:

- Leading lepton: $p_{\mathrm{T}}^{l} > 27$ GeV
- Sub-leading lepton: $p_{\mathrm{T}}^{l} > 20$ GeV
- Electron: $|\eta^{e}| < 2.47$
- Muon: $|\eta^{\mu}| < 2.4$
- $e\mu$, exactly two leptons, opposite sign
- Dilepton: $m_{ll} > 20$ GeV, $p_{\mathrm{T}}^{ll} > 30$ GeV

where the last point reflects the kinematic selection used in the analysis to suppress the background. The definition does not contain the requirement on particle activity, since we assume that the exclusive component contains only the two leptons.

The exclusive $W^{+}W^{-}$ Monte Carlo is used to determine event selection efficiency $\epsilon_{e\mu}$, which accounts for effects of the detector, e.g. trigger and reconstruction efficiencies of the leptons. It is simply defined as a ratio of reconstructed events with the complete selection except the exclusivity veto $N^{\mathrm{reco}}_{\mathrm{pre-excl.}}$ and number of true events which are in the fiducial region $N^{\mathrm{truth}}_{\mathrm{fid.}}$:

$$\epsilon_{e\mu} = \frac{N^{\mathrm{reco}}_{\mathrm{pre-excl.}}}{N^{\mathrm{truth}}_{\mathrm{fid.}}}.$$

The exclusive selection is not included in $\epsilon_{e\mu}$, since we are able to determine exclusive efficiency in data.

6.3.2 Fiducial cross-section

Finally, all factors necessary to extract the cross-section are available. The cross-section in the fiducial region is calculated using following formula:

$$\sigma^{\mathrm{Data,fid.}}_{\gamma\gamma\to W^{+}W^{-}\to e^{\pm}\mu^{\mp}} = \frac{N_{\mathrm{tot}} - N_{\mathrm{bkg}}}{L_{\mathrm{int}} \cdot \epsilon_{e\mu} \cdot \epsilon_{\mathrm{excl}}},$$

where:

- $N_{\mathrm{tot}} = 62.0 \pm 7.9$ (stat) is a total number of observed events in data,
- $N_{\mathrm{bkg}} = 29.0 \pm 6.0$ (stat) $\pm\, 1.9$ (syst) is number of simulated background events,
- $\epsilon_{\mathrm{excl}} = 0.555 \pm .009$ (syst) is exclusive efficiency measured in data. It has a negligible statistical uncertainty smaller than 0.0001.

Source of uncertainty	Relative uncertainty
Pile-up reweighting	1.2%
Luminosity	3.4%
Muon related	0.8%
Electron related	0.7%
Track related	0.2%
Exclusive efficiency	1.6%
Background modelling	7.3%
Total systematic	8.4%
Statistical	30.1%
Total uncertainty	31.2%

Table 6.2: Summary of all contributions to the total uncertainty of the fiducial cross-section, divided into the most important categories.

- $\epsilon_{e\mu} = 0.462 \pm 0.005$ (stat) $\pm\, 0.008$ (syst) is the selection efficiency, a ratio between measured events before exclusivity veto and total number of event in fiducial region,
- $L_{\text{int}} = 33.3 \pm 1.2$ (syst) fb^{-1} is total measured integrated luminosity.

Putting all these numbers together, one obtains measured cross-section:

$$\sigma^{\text{Excl.,fid.}}_{\gamma\gamma\to W^+W^-\to e^\pm\mu^\mp} = 3.9 \pm 1.2\ (\text{stat}) \pm 0.4\ (\text{syst})\ \text{fb}$$

There is no detailed study of the uncertainties for the theoretical cross-section, but preliminary value is derived using:

$$\sigma^{\text{H7,fid.}}_{\gamma\gamma\to W^+W^-\to e^\pm\mu^\mp} = \sigma^{\text{fid.}}_{\text{H7}} S_{\text{excl}},$$

where $\sigma^{\text{fid.}}_{H7}$ is the prediction of the signal Monte-Carlo Herwig 7 [51] in the fiducial region and $S_{\text{excl}} = 3.39 \pm 0.23$ is the scale factor accounting for survival factor and dissociation obtained from data.

One then gets:

$$\sigma^{\text{H7,fid.}}_{\gamma\gamma\to W^+W^-\to e^\pm\mu^\mp} = 3.85 \pm 0.02\ (\text{stat}) \pm 0.37\ (\text{syst})\ \text{fb},$$

where the source of uncertainty is currently only reflecting the uncertainty of the scale factor and exclusive efficiency and it is underestimating contribution of other factors.

6.3.3 Summary of uncertainties

Contribution of all uncertainties is summarized in Table 6.2, with total systematic uncertainty being 8.4%. The dominant contribution comes from background modelling, followed by pile-up reweighting, luminosity and exclusive efficiency. In contrast, track related uncertainties are negligible.

The statistical uncertainties amount to 30.1%, with total uncertainty being 31.2%.

6.4 Discussion of the results

The cross-section was measured in fiducial region defined by detector acceptance and kinematic selection. After application of all corrections, the measured cross-section is in agreement with the predicted cross-section within the total uncertainty. The agreement is also visible in the differential distributions shown in Section 6.2.

The total uncertainty is around 31% and is dominated by the statistical uncertainty in Monte Carlo and data. Still, the analysis has 3 times more events than the previous measurement at 8 TeV and the overall uncertainty is smaller and it therefore provides good additional validation of the Standard Model. The uncertainty will be reduced when Monte Carlo production with larger statistics is available. Furthermore, an optimization of selection could improve signal to background ratio.

Additional data taking could also lead to further improvement of the precision; however, with larger pile-up the signal will be more suppressed due to lower exclusive efficiency. Furthermore, it could be more difficult to constrain background with larger pile-up.

Chapter 7

The photon-induced dilepton measurement

In this chapter, analysis of exclusive dilepton production at 13 TeV is presented. Advantage of this photon-induced process is that it has high yield and is easy to select, since there are only two leptons in the final state. Those leptons are mostly back-to-back due to low virtuality of the interacting photons.

Because of the easy selection of the dilepton production, it is useful as a standard candle of the exclusive measurements. Aside from confirmation of the Standard Model, study of the dilepton final state is used to determine the survival factor and its dependence on kinematics.

The analysis considers only data recorded during the 2015 run at 13 TeV. The conditions at the time allowed to use triggers with a low threshold on lepton p_{T}. It was therefore possible to study the dilepton production at lower values of p_{T} and lower dilepton invariant mass $m_{\mu\mu}$. It was also possible to study differentially the cross-section as a function of $m_{\mu\mu}$. The analysis only studied dimuon final state.

Aside from me, the 13 TeV analysis was performed by a small group of four people and is summarized in ATLAS internal note [69] and paper draft [70]. I contributed mainly to the following parts of the analysis:

- Validation and studies of exclusive photon-induced Monte Carlo
- Preliminary extraction of the survival factor
- Derivation of trigger efficiency in Monte Carlo and its validation

The goal of this chapter is therefore to summarize the analysis with the emphasis on aspects of the analysis I worked on.

The dilepton measurement is in many ways similar to the diboson analysis. The final state particles are the same, the main difference being that the leptons in the final state of the dilepton analysis must have the same flavour and there is no momentum carried away by the neutrinos from W decays.

The first stage of the analysis includes lepton preselection, used mainly for studies and validation of various MC corrections. To isolate the signal, an exclusive selection is used, which requires no tracks in vicinity of the dilepton vertex. After isolation of the signal, it was possible to study the survival factor and determine the cross-section.

To avoid duplication of text, aspects of the analysis which are the same or similar to the diboson analysis are only shortly mentioned and appropriate section in the diboson part is cited if necessary.

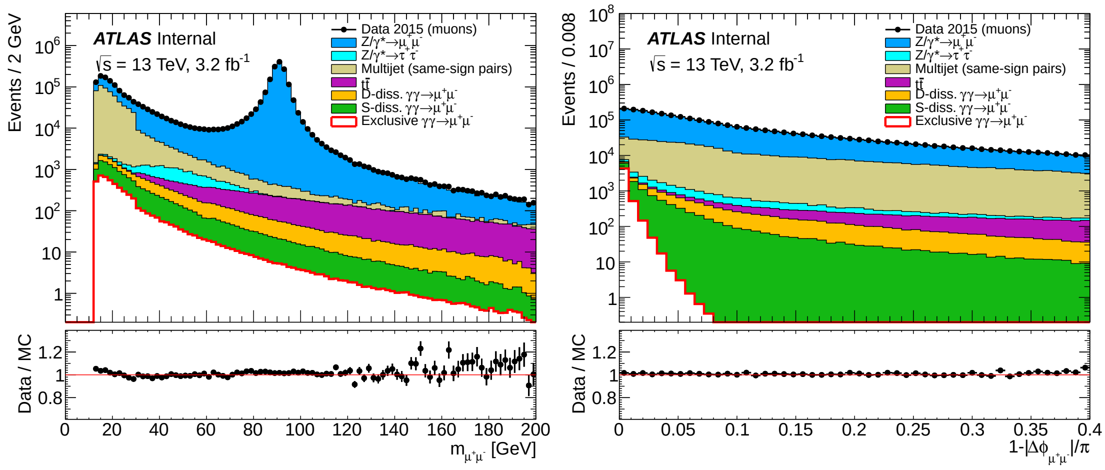

(a) (b)

Figure 7.1: (a) Invariant mass $m_{\mu\mu}$ and (b) acoplanarity distributions after preselection.

7.1 Overview of Monte Carlo generators

The elastic component of the $\gamma\gamma \to l^+l^-$ was generated using Herwig++ [55], the single-dissociative was done with LPair 4.0 [56] and the double dissociative with Pythia 8 [53]. Unlike the diboson analysis, the dilepton measurement considers the dissociative contribution to be a background.

One of my responsibilities was to test production of the elastic and double dissociative component of the Monte Carlo. For the latter, several configurations of the Monte Carlo were studied.

Another significant background to the elastic component is the Drell-Yan process with dimuon final state and $t\bar{t}$ production, both generated using PowHeg [52] interfaced with Pythia generator [53].

7.2 Preselection

First, events which were not properly recorded or have no defects in terms of quality are omitted from the analysis. Then, several dimuon triggers are used:

- Trigger requiring two muons with $p_{\mathrm{T}} > 10$ GeV used for events with $m_{\mu\mu} > 30$ GeV.
- Trigger requiring two muons with $p_{\mathrm{T}} > 6$ GeV used for events with $m_{\mu\mu} < 30$ GeV.

Trigger with $p_{\mathrm{T}} > 4$ GeV was also studied but its contribution to the total number of events was negligible and it was therefore omitted.

Muons are selected using the selection described in Section 4.2.1, where the selection on transverse momentum is changed to $p_{\mathrm{T}}^{\mu} > 6$ GeV. Finally, two selected muons with an opposite charge are required.

Distributions of data and signal and background Monte Carlo generators are displayed in Figure 7.1. Aside from the fact that the Monte Carlo predictions are in good correspondence with data, one can also notice a concentration of exclusive events in lower values of acoplanarity ($aco = 1 - |\Delta\phi_{\mu\mu}|/\pi$) thanks to the fact that the two leptons are produced back-to-back. The exclusive events form only a negligible portion of the events and careful selection needs to be implemented to select events of interest.

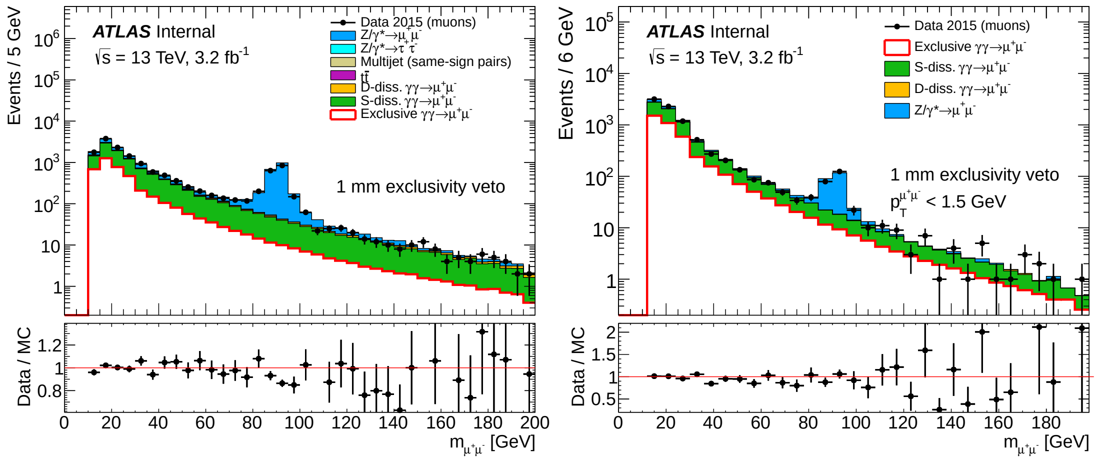

(a) (b)

Figure 7.2: Invariant mass $m_{\mu^+\mu^-}$ after (a) exclusivity veto and (b) cut on $p_{\mathrm{T}}^{\mu^+\mu^-} < 1.5$ GeV.

7.3 Exclusive selection

The background after the preselection is dominated by processes which are accompanied by an additional particle production. Since the signal only produces two leptons, it can be isolated using selection on this additional activity.

The exclusive selection requires only events with no additional particle within 1 mm from the dilepton vertex. Distribution of the invariant mass after the selection can be found in Figure 7.2a. The distributions are now dominated by exclusive and single-dissociative components aside from the peak at mass of the Z boson.

7.4 Additional selection

Another useful property of the exclusive dilepton production is that the leptons are typically back-to-back. Signal events are therefore concentrated at lower values of dilepton transverse momentum and at lower values of acoplanarity.

Requiring $p_{\mathrm{T}}^{\mu\mu} < 1.5$ GeV or $aco < 0.008$ leads to good isolation of the signal. We used selection on the transverse momentum, the dimuon invariant mass spectra after its application can be found in Figure 7.2b.

The background is now dominated by the single-dissociative component and by the Drell-Yan contribution in the Z mass region. It is therefore useful to exclude the region $70 < m_{\mu\mu} < 105$ GeV from the analysis, making the Drell-Yan contribution negligible. The single dissociative component is a non-reducible background. Most of the components of the proton dissociation are outside the kinematic range of the ATLAS detector and from the standpoint of the experiment the single-dissociative component is experimentally indistinguishable.

7.5 Dimuon trigger modelling

One of the corrections applied to MC is the trigger scale factor, which compensates for difference between trigger efficiency in data and Monte Carlo. While for the high-p_{T}

trigger the corrections was determined centrally by muon performance group, in case of the low-p_{T} triggers it had to be derived. First, the trigger efficiency in data and Monte Carlo is determined. The scale factor is then taken simply as a ratio of these efficiencies.

The procedure used to determine an efficiency of a dimuon trigger is to derive trigger efficiency of a single muon $\epsilon_{match,\mu}(p_{\mathrm{T}}, q\eta)$ (where q is the charge of the muon). The dimuon trigger efficiency is then defined as:

$$\epsilon_{trig,dimuon} = \epsilon_{match,\mu}(p_{T,1}, q_1\eta_1) \cdot \epsilon_{match,\mu}(p_{T,2}, q_2\eta_2) \cdot C$$

where C is a correlation factor. Effect of the correlation is only significant if the two muons are close to each other and there is an overlap of information used by the trigger. For muons separated by a significant distance this factor is simply 1. Since in the analysis the muons are back-to-back, this is a very good approximation.

7.5.1 Tag-and-probe method

The Tag-and-probe is a method often used at the LHC to derive efficiencies of various objects of interest. They take advantage of decays of particles. In case of two muons, this can be for example J/Ψ, Υ or Z resonance.

The idea is to use a pair of leptons originating from the resonances (this is achieved by a requirement on the invariant mass of the leptons) where one muon has to pass some additional requirement (e.g. some trigger). This muon is called *tag*, because it is used to tag events which are used to determine the efficiency.

The second muon is called *probe* and is used to probe the studied property. Due to the requirement on the invariant mass and on the tag muon, the probe muons mostly originate from the resonance decay. One therefore has muons without significant contamination of the sample from fake and secondary muons. When studying trigger efficiency, one simply studies probability of the probe muon passing requirement of the trigger.

For this study, a tool made by Dai Kobayashi was used (more information can be found in [62]) and the efficiency was derived for trigger `HLT_mu6` (which requires one muon with $p_{\mathrm{T}} > 6$ GeV). J/Ψ was used as the resonance particle, where the two muons were required to have invariant mass within 100 MeV of J/Ψ mass. *Upsilon* resonance was used as a cross-check.

The tag muon was then required to pass a trigger requiring $p_{\mathrm{T}}^{\mu} > 4$ GeV. The efficiency, taken as a function of muon p_{T} and $q\eta$, is then the fraction of matched probe muons and all probe muons:

$$\epsilon_{\mathrm{HLT\_mu6}}(p_{\mathrm{T}}, q\eta) = \frac{N_{probe}^{pass}(p_{\mathrm{T}}, q\eta)}{N_{probe}^{all}(p_{\mathrm{T}}, q\eta)}$$

The whole process is slightly complicated by the fact that for large energies of the J/ψ the resulting muons are really close to each other and in order to eliminate correlation when information from both particles is overlying (which is a situation not applicable to our analysis, where the muons are back-to-back), a selection on distance $\Delta R = \sqrt{\Delta\eta^2 + \Delta\phi^2} > 0.2$ is introduced.

The resulting efficiency for Monte Carlo and data is in Figures 7.3 and 7.3b. The efficiency is in both cases lower for muons with lower values of p_{T}. There are significant drops in efficiency in regions with detector imperfection (e.g. there is a gap in the muon spectrometer for $\eta = 0$).

Finally, ratio of data- and MC-trigger efficiencies gives the necessary scale factor, which can be found in Figure 7.3c. A larger difference between data is found for central values

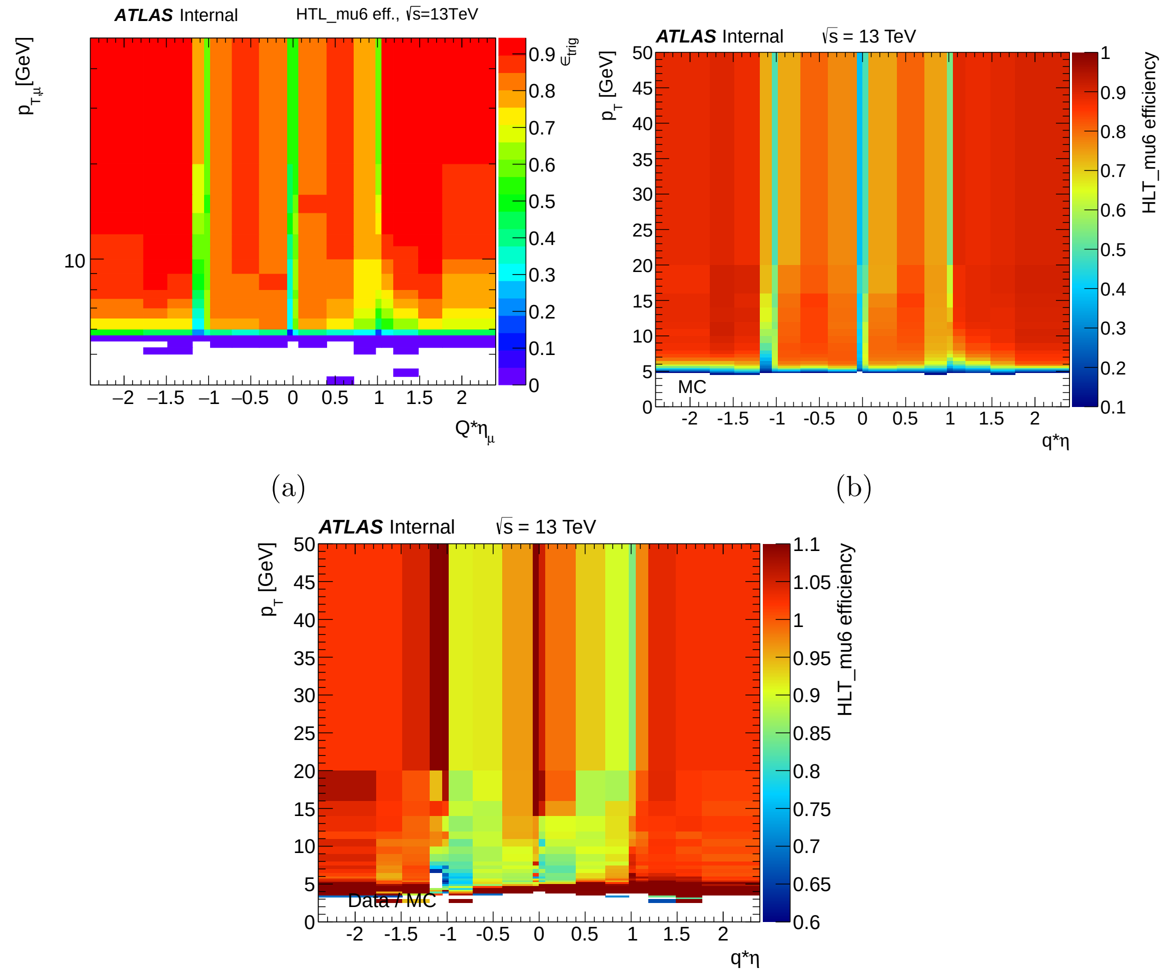

(a) (b) (c)

Figure 7.3: Trigger efficiency of `HLT_mu6` derived using (a) Monte Carlo, (b) data. (c) scale factor, taken as ratio of data and Monte Carlo trigger efficiencies.

of pseudorapidity, where the difference is around 10% and in low values of p_{T}. The largest difference is found at low-p_{T} region at $\eta = -1$.

7.5.2 Inclusive trigger efficiency

In order to validate the results determined using Tag and Probe, an alternative method was used. It uses more simple and direct approach. Using the same events as used in previous case, one muon is checked whether it fired the trigger. Ratio of events where the muon fired the studied trigger and all selected events is then taken as the efficiency.

This method is not as robust as the TaP method, since it is more sensitive to e.g. fake muons, but still it gives compatible results, as can be seen in Figure 7.4. This method is only used in Monte Carlo and not data, since MC does not contain background.

7.5.3 Systematic uncertainties

Two sources of systematic uncertainties were studied:

Mass window variation: The size of the mass windows used to select muon pairs

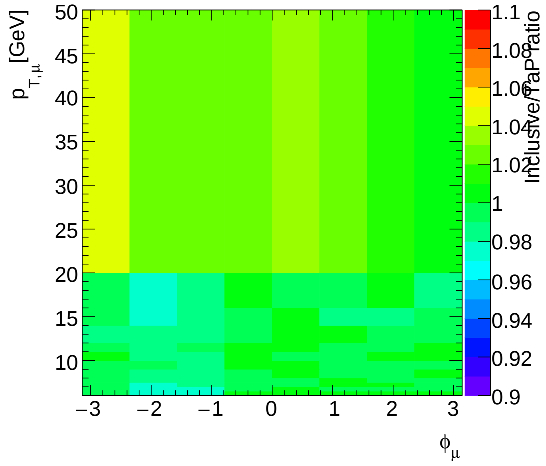

Figure 7.4: Ratio of inclusive and TaP trigger efficiencies for the `HLT_mu6` trigger.

is expanded by additional 100 MeV, which leads to higher contribution of background. Effect on the results is found to be at most 0.5%.

Alternative application: Instead of application of the scale factor as a function of p_{T} and $q\eta$, it is applied as a function of ϕ and $q\eta$. The difference in the measured cross-section is taken as an additional uncertainty and is found to be 0.9%.

7.6 Results

The full sample from 2015 run has integrated luminosity of 3.21 fb^{-1} with relative uncertainty 2.1%, comparable to 7 TeV. However, 3 times more events are observed, since the low p_{T} muon triggers were included. This results in more precise measurement and possibility to study kinematic properties of the survival factor.

The survival factor was measured by a likelihood fit for the phase-space identified by the $p_{\mathrm{T}}^{\mu\mu} < 1.5$ GeV requirement, where the fit is done in acoplanarity. The survival factor was found to be:

$$S^{\mathrm{excl}}_{\gamma\gamma\to\mu\mu} = 0.883 \pm 0.020\ (\mathrm{stat}).$$

Control distributions with applied scale factor can be found in Figure 7.5, showing good differential agreement between data and Monte Carlo.

7.6.1 Systematic uncertainties

Full discussion of the systematic uncertainties is outside the scope of this thesis. Main contributors are:

Muon related contribution comes mainly from uncertainties of the scale factors and contribute 1.6% to the total systematic uncertainty.

Modelling of exclusivity veto uncertainty comes from uncertainty of the exclusive efficiency and its effect on the cross-section is 1.2%.

Luminosity uncertainty comes from the van der Meer scan and contributes 2.1% to the total uncertainty.

The total systematic uncertainty of the measurement is found to be 3.2%.

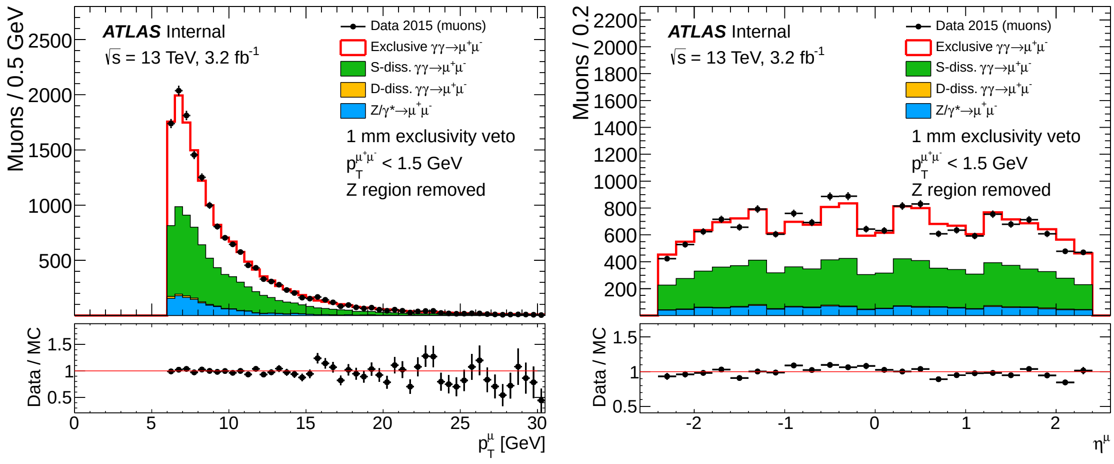

(a) (b)

Figure 7.5: Control distributions of (a) muon transverse momentum and (b) muon pseudorapidity after exclusive selection, with the exclusive dilepton Monte Carlo scaled by the survival factor.

7.6.2 Cross-section

The cross-section is measured in the following fiducial region:

- 12 GeV $< m_{\mu\mu} <$ 30 GeV, with $p_{\mathrm{T}}^{\mu} > 6$ GeV, $|\eta| < 2.4$
- 30 GeV $< m_{\mu\mu}$, with $p_{\mathrm{T}}^{\mu} > 10$ GeV, $|\eta| < 2.4$

The p_{T} selection is mainly driven by the triggers, while the η is limited by the geometry of the detector.

The cross-section for given fiducial region is determined using the following formula:

$$\sigma_{excl} = \frac{N_{obs} - N_{bkg}}{L_{\mathrm{int}} \cdot \epsilon^{\mu\mu} \cdot \epsilon^{excl} \cdot A^{\mu\mu}},$$

where N_{obs} is the number of observed events, N_{bkg} is the number of background events (estimated from MC after application of survival factor), the L_{int} represents the integrated luminosity. $\epsilon^{\mu\mu}$ stands for the efficiency to reconstruct dimuon pair and it accounts for muon reconstruction efficiency, trigger efficiency etc. The ϵ^{excl} accounts for reduction of events due to the exclusive selection and $A^{\mu\mu}$ is the same but for the remaining selection (Z mass peak removal, $p_{\mathrm{T}}^{\mu\mu} < 1.5$ GeV).

In our case those values are:

- $N_{obs} - N_{bkg} = 3880 \pm 90$ (stat.)
- $L_{\mathrm{int}} = 3.19 \pm 0.07$ fb
- $\epsilon^{\mu\mu} = 0.405 \pm 0.007$ (syst.)
- $\epsilon^{\mathrm{excl.}} = 0.794 \pm 0.012$ (syst.)
- $A^{\mu\mu} = 0.964$

Putting everything together one arrives at a cross-section:

$$\sigma^{\text{excl. fid.}}_{\gamma\gamma\rightarrow\mu^+\mu^-} = 3.22 \pm 0.07\ (\text{stat}) \pm 0.10\ (\text{syst})\ \text{pb}.$$

The theoretical cross-section of EPA corrected for absorptive effects [71] is then found to be: $\sigma^{\text{EPA, corr.}}_{\gamma\gamma\rightarrow\mu^+\mu^-} = 3.14 \pm 0.05$ pb, a value compatible with the measured results. The cross-section was also derived using SuperChic2 generator [72]: $\sigma^{\text{SC2}}_{\gamma\gamma\rightarrow\mu^+\mu^-} = 3.45 \pm 0.05$ pb.

7.6.3 Differential cross-section

Since the 2015 data provide a sufficient yield, it is possible to study the cross-section differentially.

A formula used to define the cross-section is:

$$\left(\frac{\mathrm{d}\sigma^{\text{excl.}}_{\gamma\gamma\rightarrow\mu^+\mu^-}}{\mathrm{d}m_{\mu\mu}}\right)_i = \frac{(N_{\text{obs}} - N_{\text{bkg}})_i}{L_{\text{int}} \cdot \epsilon^{\text{excl.}} \cdot \epsilon_i^{\mu\mu} \cdot A_i^{\mu\mu} \cdot (\Delta m)_i}. \tag{7.1}$$

where i refers to i-th mass bin. The variables are similar to the case of total cross-section, but measured as a function of mass. $(N_{\text{obs}} - N_{\text{bkg}})_i$ is the number of measured signal events, $\epsilon_i^{\mu\mu}$ is the efficiency, $\epsilon_i^{\text{excl.}}$ the exclusivity efficiency and $A_i^{\mu\mu}$ is the acceptance factor. Finally, $(\Delta m)_i$ is width of the mass bin.

The measured cross-section as a function of the invariant mass can be found in Figure 7.6, together with several predicted values. The EPA prediction with absorptive effects from Ref. [71] is in good agreement with the measured values up to $m_{\mu\mu} = 30$ GeV, while the SuperChic prediction [72] deviates quite a lot in that region.

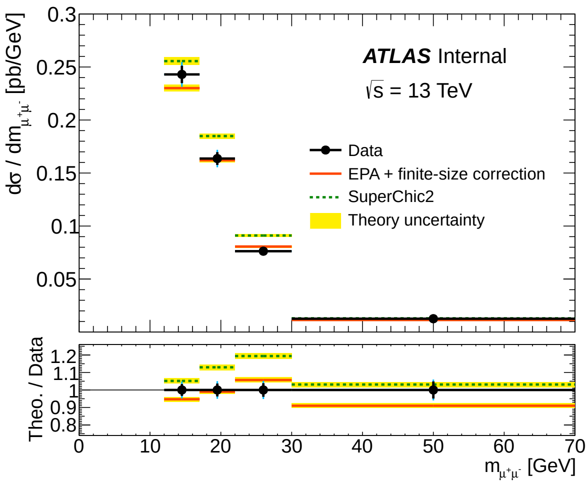

Figure 7.6: The differential cross-section of the exclusive dilepton production a a function of the dimuon invariant mass. Aside from measured cross-section, predictions by SuperChic2 Monte Carlo and by EPA with absorptive effects are also displayed.

Summary

Study of the photon-induced processes is an important as a test of the Standard Model and can be also used for beyond Standard Model searches. In this thesis, two processes are considered. The measurements were performed with ATLAS at the Large Hadron Collider at center-of-mass energies $\sqrt{s} = 13$ TeV. Primary focus of the thesis is analysis of exclusive production of WW with $e\mu$ in final state, where I contributed the most. The second analysis deals with the exclusive production of two muons in the final state. The description of the analysis is emphasising personal contribution to the analysis.

Necessary theoretical background was presented in the first chapter, focusing on the Standard Model and photon-induced processes. This was followed by a description of equivalent photon approximation in Chapter 2. The approximation provides a framework to calculate photon-photon interactions in collisions of charged particles. It also reviewed previous measurements of the $\gamma\gamma \to l^+l^-$ and $\gamma\gamma \to W^+W^-$ productions.

In the third chapter, the ATLAS detector is described in detail and includes a short description of the lepton reconstruction strategy.

Discussions of the diboson measurement spans Chapters 4-7. The strategy used in diboson analysis is outlined in Chapter 4. Data and Monte Carlo production used in the analysis are introduced, together with general corrections of Monte Carlo. The signal is isolated based on track activity in proximity of the dilepton vertex. Analysis-specific corrections of Monte Carlo are presented in Chapter 6. They are mainly designed to constrain the background and to estimate the fraction of the signal for the absence of dissociation and of the survival factor.

Chapter 7 shows results of the analysis and summarizes systematic uncertainties contributing to the final measurement. Differential distributions are presented, which show good compatibility between data and Monte Carlo. The measured fiducial cross-section is found to be $\sigma^{\text{Excl.,fid.}}_{\gamma\gamma\to W^+W^-\to e^\pm\mu^\mp} = 3.9 \pm 1.2\ (\text{stat}) \pm 0.4\ (\text{syst})$ fb. It is in agreement with the theoretical prediction $\sigma^{\text{H7,fid.}}_{\gamma\gamma\to W^+W^-\to e^\pm\mu^\mp} = 3.85 \pm 0.02\ (\text{stat}) \pm 0.37\ (\text{syst})$ fb .

The final chapter summarizes the dilepton analysis. My contribution to the measurement is mainly Monte Carlo validation and low-p_T trigger scale factor determination. The survival factor, which describes reduction of the cross-section due to additional interaction between the protons, is found to be $S^{\text{excl}}_{\gamma\gamma\to\mu\mu} = 0.883 \pm 0.020(\text{stat})$. This leads to cross-section of exclusive dimuon production $\sigma^{\text{excl. fid.}}_{\gamma\gamma\to\mu^+\mu^-} = 3.22 \pm 0.07\ (\text{stat}) \pm 0.10\ (\text{syst})$ pb, which is in agreement with predictions $\sigma^{\text{EPA, corr.}}_{\gamma\gamma\to\mu^+\mu^-} = 3.14 \pm 0.05$ pb and $\sigma^{\text{SC2}}_{\gamma\gamma\to\mu^+\mu^-} = 3.45 \pm 0.05$ pb. Differential cross-section is presented as well.

Appendix A - Additional preselection figures

Additional distributions of data and Monte Carlo after the preselection described in Section 4.2. In Figure 7.7 are distributions of invariant mass and dilepton p_T fo the $\mu\mu$ channel. Figure 7.8 presents properties of the electron and muon from the $e\mu$ pair.

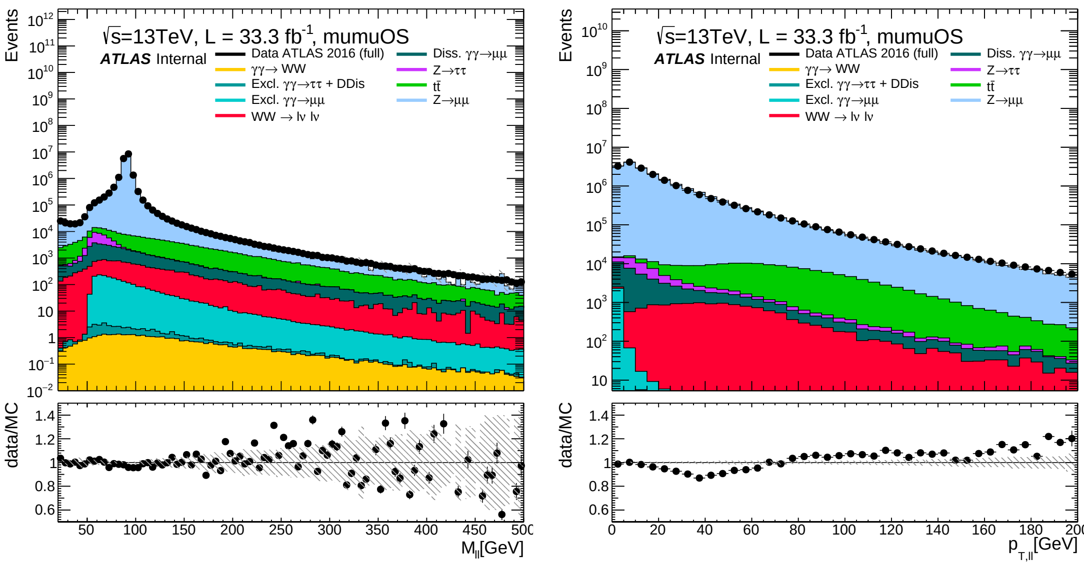

(a)

(b)

Figure 7.7: Distributions of data and Monte Carlo as a function of a) invariant mass and b) leading electron p_T for $\mu\mu$ channel after the preselection.

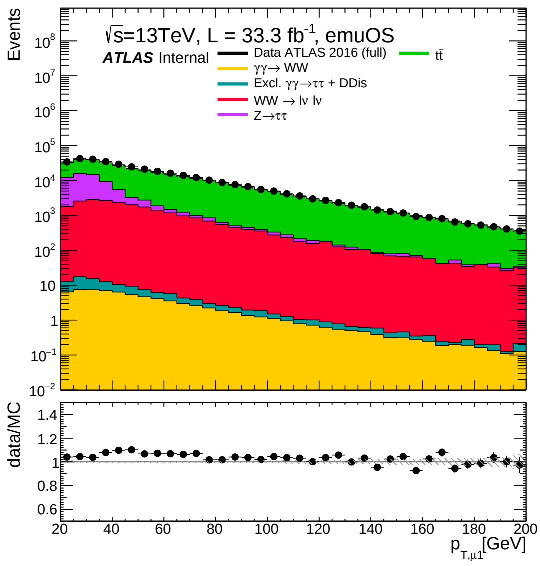

(1a)

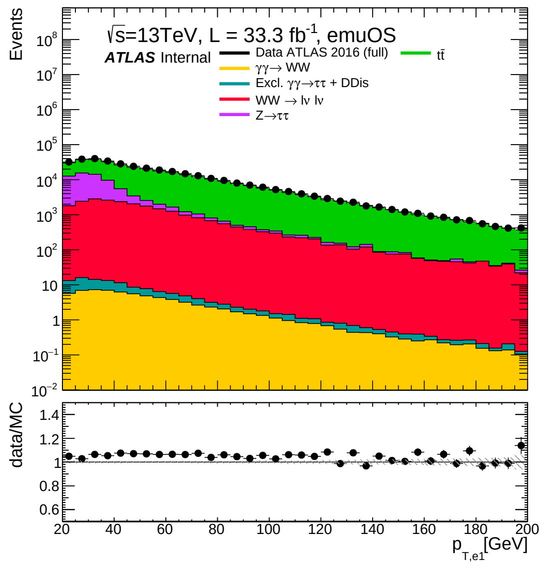

(1b)

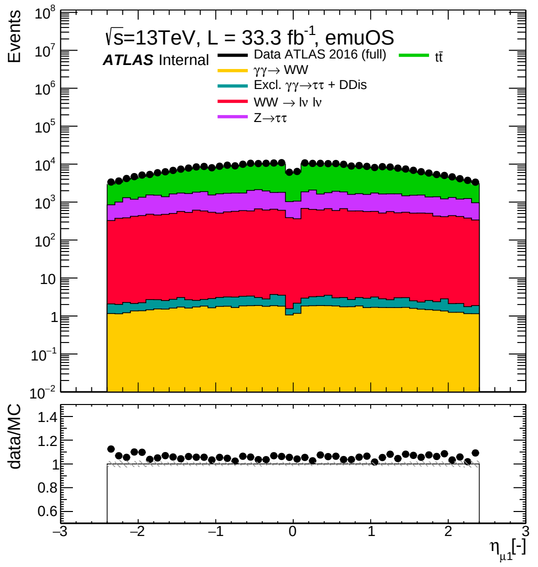

(2a)

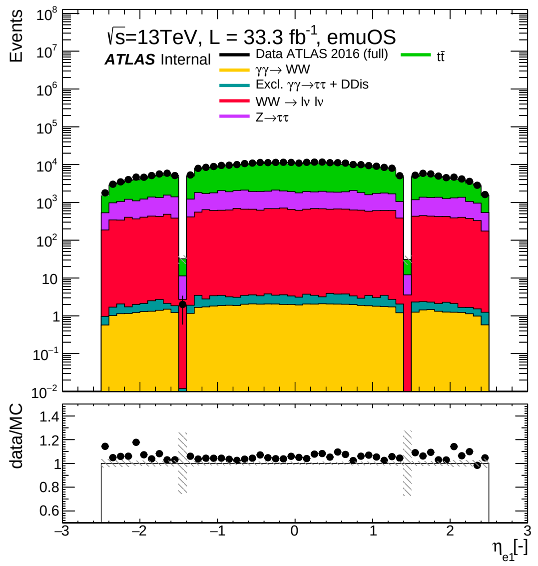

(2b)

Figure 7.8: Distributions of data and Monte Carlo as a function of 1) transverse momentum p_{T} and 2) pseudorapidity η of a) muon and b) electron from the dilepton pair in the $e\mu$ channel after the preselection.

Bibliography

[1] David Griffiths, " Introduction to Elementary Particles," Wiley, 2008, 470 ISBN: 978-3-527-40601-2

[2] Glenn F. Knoll, "Radiation Detection and Measurement," John Wiley & Sons, 16. 8. 2010

[3] L. Bergstrom, "Saas-Fee Lecture Notes: Multi-messenger Astronomy and Dark Matter," arXiv:1202.1170 [astro-ph.CO].

[4] Group Serra, Standard Model, http://www.physik.uzh.ch/groups/serra/StandardModel.html

[Cited on 7. 4. 2016]

[5] P. Achard *et al.* [L3 Collaboration], "Measurement of the running of the electromagnetic coupling at large momentum-transfer at LEP," Phys. Lett. B **623** (2005) 26 doi:10.1016/j.physletb.2005.07.052 [hep-ex/0507078].

[6] P. Skands, "Introduction to QCD," [arXiv:1207.2389 [hep-ph]].

[7] ATLAS Collaboration, "Observation of a new particle in the search for the Standard Model Higgs boson with the ATLAS detector at the LHC," Phys. Lett. B **716** (2012) 1 doi:10.1016/j.physletb.2012.08.020

[arXiv:1207.7214 [hep-ex]].

[8] CMS Collaboration, "Observation of a new boson at a mass of 125 GeV with the CMS experiment at the LHC," Phys. Lett. B **716** (2012) 30 doi:10.1016/j.physletb.2012.08.021

[arXiv:1207.7235 [hep-ex]].

[9] L. D. Landau and E. M. Lifschitz, "Production of electrons and positrons by a collision of two particles," Phys. Z. Sowjetunion **6** (1934) 244.

[10] S. J. Brodsky, T. Kinoshita and H. Terazawa, "Two Photon Mechanism of Particle Production by High-Energy Colliding Beams," Phys. Rev. D **4** (1971) 1532. doi:10.1103/PhysRevD.4.1532

[11] F. Krauss, M. Greiner and G. Soff, "Photon and gluon induced processes in relativistic heavy ion collisions," Prog. Part. Nucl. Phys. **39** (1997) 503. doi:10.1016/S0146-6410(97)00049-5

[12] A.I. Nikishov, "Absorption of High-Energy Photons in the Universe," JETP **14** (1962) 393.

[13] T. Piran, "The physics of gamma-ray bursts," Rev. Mod. Phys. **76** (2004) 1143 doi:10.1103/RevModPhys.76.1143

[astro-ph/0405503].

[14] ATLAS public results, "Measurement of exclusive $\gamma\gamma \rightarrow W^+W^-$ production and search for exclusive Higgs boson production in pp collisions at $\sqrt{s} = 8$ TeV using the ATLAS detector," https://atlas.web.cern.ch/Atlas/GROUPS/PHYSICS/PAPERS/STDM-2015-10/

[Cited on 22. 4. 2017]

[15] E. Chapon, C. Royon, and O. Kepka, "Anomalous quartic $WW\gamma\gamma$, $ZZ\gamma\gamma$ and trilinear $WW\gamma$ couplings in two-photon processes at high luminosity at the LHC," Phys. Rev. D81 (2010) .

[16] A. Denner, S. Dittmaier and R. Schuster, "Radiative corrections to $\gamma\gamma \rightarrow W^+W^-$ in the electroweak standard model," Nucl. Phys. B **452** (1995) 80 doi:10.1016/0550-3213(95)00344-R

[hep-ph/9503442].

[17] F. Moulin, D. Bernard and F. Amiranoff, "Photon-photon elastic scattering in the visible domain," Z. Phys. C **72** (1996) 607. doi:10.1007/s002880050282

[18] D. Bernard *et al.*, "Search for Stimulated Photon-Photon Scattering in Vacuum," Eur. Phys. J. D **10** (2000) 141 doi:10.1007/s100530050535

[arXiv:1007.0104 [physics.optics]].

[19] ATLAS Collaboration, "Light-by-light scattering in ultra-peripheral Pb+Pb collisions at $\sqrt{s_{NN}} = 5.02$ TeV with the ATLAS detector at the LHC," ATLAS-CONF-2016-111.

[20] O. J. Pike, F. Mackenroth, E. G. Hill and S. J. Rose, "A photon-photon collider in a vacuum hohlraum," Nature Photon. **8** (2014) 434-436. doi:10.1038/nphoton.2014.95

[21] X. Ribeyre, M. Lobet, E. D'Humires, S. Jequier, V. T. Tikhonchuk and O. Jansen, "Pair creation in collision of γ-ray beams produced with high-intensity lasers," Phys. Rev. E **93** (2016) no.1, 013201 doi:10.1103/PhysRevE.93.013201

[arXiv:1504.07868 [physics.ins-det]].

[22] C. F. v. Weizsäcker, "Ausstrahlung bei Stössen sehr schneller Elektronen," Zeitschrift für Physik **88** (1934) 612

[23] E. J. Williams, "Nature of the high-energy particles of penetrating radiation and status of ionization and radiation formulae," Phys. Rev. **45** (1934) 729. doi:10.1103/PhysRev.45.729

[24] M. Dyndal, "Two-Photon Interactions in Proton−Proton Collisions with the ATLAS Experiment at the LHC," CERN-THESIS-2015-160.

[25] E. Fermi, "On the theory of collisions between atoms and electrically charged particles," Nuovo Cim. **2** (1925) 143 doi:10.1007/BF02961914

[hep-th/0205086].

[26] V. M. Budnev, I. F. Ginzburg, G. V. Meledin and V. G. Serbo, Nucl. Phys. B **63** (1973) 519. doi:10.1016/0550-3213(73)90162-4

[27] L. A. Harland-Lang, V. A. Khoze and M. G. Ryskin, JHEP **1603** (2016) 182 doi:10.1007/JHEP03(2016)182

[arXiv:1601.07187 [hep-ph]].

[28] L. A. Harland-Lang, V. A. Khoze and M. G. Ryskin, "The photon PDF in events with rapidity gaps,"

[arXiv:1601.03772 [hep-ph]].

[29] Atlas Colaboration, Measurement of exclusive $\gamma\gamma \to l^+l^-$ production in proton-proton collisions at $\sqrt{s}$=7 TeV with the ATLAS detector, Phys.Lett. B749 (2015) 242-261

[30] CMS Collaboration, "Exclusive photon-photon production of muon pairs in proton-proton collisions at $\sqrt{s} = 7$ TeV," JHEP **1201** (2012) 052 doi:10.1007/JHEP01(2012)052

[arXiv:1111.5536 [hep-ex]].

[31] CDF Collaboration, "Observation of Exclusive Electron-Positron Production in Hadron-Hadron Collisions," Phys. Rev. Lett. **98** (2007) 112001 doi:10.1103/PhysRevLett.98.112001

[hep-ex/0611040].

[32] CDF Collaboration, "Search for exclusive Z boson production and observation of high mass $p\bar{p} \to \gamma\gamma \to p + \ell\ell + \bar{p}$ events in $p\bar{p}$ collisions at $\sqrt{s} = 1.96$ TeV," Phys. Rev. Lett. **102** (2009) 222002 doi:10.1103/PhysRevLett.102.222002

[arXiv:0902.2816 [hep-ex]].

[33] CDF Collaboration, "Observation of exclusive charmonium production and $\gamma + \gamma$ to $\mu^+\mu^-$ in $p\bar{p}$ collisions at $\sqrt{s} = 1.96$ TeV," Phys. Rev. Lett. **102** (2009) 242001 doi:10.1103/PhysRevLett.102.242001

[arXiv:0902.1271 [hep-ex]].

[34] H1 Collaboration, "Muon pair production in ep collisions at HERA," Phys. Lett. B **583** (2004) 28 doi:10.1016/j.physletb.2004.01.003

[hep-ex/0311015].

[35] STAR Collaboration, Phys. Rev. C **70** (2004) 031902 doi:10.1103/PhysRevC.70.031902

[nucl-ex/0404012].

[36] PHENIX Collaboration, "Photoproduction of J/psi and of high mass e+e- in ultra-peripheral Au+Au collisions at s**(1/2) = 200-GeV," Phys. Lett. B **679** (2009) 321 doi:10.1016/j.physletb.2009.07.061

[arXiv:0903.2041 [nucl-ex]].

[37] ATLAS Collaboration, "Measurement of exclusive $\gamma\gamma \to W^+W^-$ production and search for exclusive Higgs boson production in pp collisions at $\sqrt{s} = 8$ TeV using the ATLAS detector," Phys. Rev. D **94** (2016) no.3, 032011 doi:10.1103/PhysRevD.94.032011

[38] CMS Collaboration, "Study of exclusive two-photon production of W^+W^- in pp collisions at $\sqrt{s} = 7$ TeV and constraints on anomalous quartic gauge couplings," JHEP **1307** (2013) 116 doi:10.1007/JHEP07(2013)116

[arXiv:1305.5596 [hep-ex]].

[39] CMS Collaboration, "Evidence for exclusive gamma-gamma to W+ W- production and constraints on Anomalous Quartic Gauge Couplings at sqrt-s = 8 TeV," CMS-PAS-FSQ-13-008.

[40] Stephen Myers, "The large hadron collider 2008-2013," Int. J. Mod. Phys. A, **28** (2013) 1330035 [DOI: 10.1142/S0217751X13300354].

[41] S. van der Meer, "Calibration of the Effective Beam Height in the ISR," CERN-ISR-PO-68-31.

[42] [ATLAS Collaboration], G. Aad *et al.* "Luminosity Determination Using the ATLAS Detector," ATLAS-CONF-2010-060. CERN-THESIS-2014-035

[43] G. Aad *et al.* [ATLAS Collaboration], "Studies of the performance of the ATLAS detector using cosmic-ray muons," Eur. Phys. J. C **71** (2011) 1593

[arXiv:1011.6665 [physics.ins-det]].

[44] ATLAS Public Results, "LuminosityPublicResultsRun2," https://twiki.cern.ch/twiki/bin/view/AtlasPublic/LuminosityPublicResultsRun2,

[Cited on 2. 5. 2017]

[45] G. Aad *et al.* [ATLAS Collaboration], "The ATLAS Experiment at the CERN Large Hadron Collider," JINST **3** (2008) S08003.

[46] G. Aad *et al.* [ATLAS Collaboration], Phys. Lett. B **758** (2016) 67 doi:10.1016/j.physletb.2016.04.050 [arXiv:1602.01633 [hep-ex]].

[47] L. de Nooij, "The $\Phi(1020)$-meson production cross section measured with the ATLAS detector at $\sqrt{s} = 7$ TeV," CERN-THESIS-2014-035.

[48] M. Limper, "Track and Vertex Reconstruction in the ATLAS Inner Detector," Amsterdam, Netherlands: Eigenverl. (2009).

[49] Giordani, M, "Overview of the ATLAS Insertable B-Layer (IBL) Project," ATL-INDET-SLIDE-2012-428.

[50] L. Fiorini, "Top-Quark Physics Results From LHC,"

[arXiv:1201.5844 [hep-ex]].

[51] J. Bellm *et al.*, "Herwig 7.0/Herwig++ 3.0 release note," Eur. Phys. J. C **76** (2016) no.4, 196 doi:10.1140/epjc/s10052-016-4018-8

[arXiv:1512.01178 [hep-ph]].

[52] C. Oleari, "The POWHEG-BOX," Nucl. Phys. Proc. Suppl. **205-206** (2010) 36 doi:10.1016/j.nuclphysbps.2010.08.016

[arXiv:1007.3893 [hep-ph]].

[53] T. Sjostrand, S. Mrenna and P. Z. Skands, "A Brief Introduction to PYTHIA 8.1," Comput. Phys. Commun. **178** (2008) 852 doi:10.1016/j.cpc.2008.01.036

[arXiv:0710.3820 [hep-ph]].

[54] J. Alwall, M. Herquet, F. Maltoni, O. Mattelaer and T. Stelzer, "MadGraph 5 : Going Beyond," JHEP **1106** (2011) 128 doi:10.1007/JHEP06(2011)128

[arXiv:1106.0522 [hep-ph]].

[55] M. Bahr *et al.*, "Herwig++ Physics and Manual," Eur. Phys. J. C **58** (2008) 639 doi:10.1140/epjc/s10052-008-0798-9

[arXiv:0803.0883 [hep-ph]].

[56] J. Vermaseren, "Two Photon Processes at Very High-Energies," Nucl.Phys. B229 (1983) 347.

[57] S. Agostinelli *et al.* [GEANT4 Collaboration], "GEANT4: A Simulation toolkit," Nucl. Instrum. Meth. A **506** (2003) 250. doi:10.1016/S0168-9002(03)01368-8

[58] G. Aad *et al.* [ATLAS Collaboration], "Muon reconstruction performance of the ATLAS detector in proton–proton collision data at $\sqrt{s}$ =13 TeV," Eur. Phys. J. C **76** (2016) no.5, 292 doi:10.1140/epjc/s10052-016-4120-y

[arXiv:1603.05598 [hep-ex]].

[59] G. Aad *et al.* [ATLAS Collaboration], "Electron reconstruction and identification efficiency measurements with the ATLAS detector using the 2011 LHC proton-proton collision data," Eur. Phys. J. C **74** (2014) no.7, 2941 doi:10.1140/epjc/s10052-014-2941-0

[arXiv:1404.2240 [hep-ex]].

[60] G. Aad *et al.* [ATLAS Collaboration], "Measurement of distributions sensitive to the underlying event in inclusive Z-boson production in *pp* collisions at $\sqrt{s} = 7$ TeV with the ATLAS detector," Eur. Phys. J. C **74** (2014) no.12, 3195 doi:10.1140/epjc/s10052-014-3195-6

[arXiv:1409.3433 [hep-ex]].

[61] Aaron Armbruster, Kevin Kröninger, Bogdan Malaescu, Francesco Spano, "Practical considerations for unfolding,"

[62] Dai Kobayashi, "Summary of J/Ψ Tag&Probe,"

https://drive.google.com/file/d/0B_ZLvkcWOdDnUTZia1l5dHRmSjQ/edit,

[Cited on 13. 5. 2016]

[63] Glen Cowan, "Statistical Data Analysis," Clarendon Press, 1998

[64] Wouter Verkerk, "Parameter estimation χ^2 and likelihood (presentation),"

https://www.physik.hu-berlin.de/de/gk1504/block-courses/autumn-2010/program_and_talks/Verkerke_part3,

[Cited on 21. 5. 2016]

[65] ROOT official website,
https://root.cern.ch/,
[Cited on 21. 5. 2016]

[66] MINUIT official website,
http://seal.web.cern.ch/seal/snapshot/work-packages/mathlibs/minuit/,
[Cited on 21. 5. 2016]

[67] RooFit official website,
http://roofit.sourceforge.net/,
[Cited on 21. 5. 2016]

[68] ATLAS internal, "LuminosityForPhysics, "
https://twiki.cern.ch/twiki/bin/view/Atlas/LuminosityForPhysics,
[Cited on 1. 5. 2017]

[69] M. Dyndal, O. Kepka, M. Stewart, F. Nechansky, E. Sauvan and L. Schoeffel, "Measurement of exclusive two-photon production of muon pairs in pp collisions at $\sqrt{s} = 13$ TeV with the ATLAS detector," CERN, Geneva (2016) ATL-COM-PHYS-2016-73

[70] M. Dyndal, O. Kepka, M. Stewart, F. Nechansky, E. Sauvan and L. Schoeffel, "Measurement of Exclusive $\gamma\gamma \to \mu\mu$ Cross Sections in Proton–Proton Collisions at $\sqrt{s} = 13$ TeV with the ATLAS Detector," Paper draft, CERN, Geneva (2017) ATL-COM-PHYS-2017-209

[71] G. Aad *et al.* [ATLAS Collaboration], "The role of finite-size effects on the spectrum of equivalent photons in proton-proton collisions at the LHC," Phys.Lett. **B741** (2015) doi:10.1016/j.physletb.2014.12.019
[arXiv:1410.298[hep-ex]].

[72] L. A. Harland-Lang, V. A. Khoze and M. G. Ryskin, "Exclusive physics at the LHC with SuperChic 2," Eur. Phys. J. C **76** (2016) no.1, 9 doi:10.1140/epjc/s10052-015-3832-8 [arXiv:1508.02718 [hep-ph]].